

# One-third of Southern Ocean productivity is supported by dust deposition

<https://doi.org/10.1038/s41586-024-07366-4>

Received: 17 April 2023

Accepted: 28 March 2024

Published online: 15 May 2024

 Check for updates

Jakob Weis<sup>1,2</sup>✉, Zanna Chase<sup>1,3</sup>, Christina Schallenberg<sup>4,5</sup>, Peter G. Strutton<sup>1,2,3</sup>, Andrew R. Bowie<sup>1,4</sup> & Sonya L. Fiddes<sup>1,2,4</sup>

Natural iron fertilization of the Southern Ocean by windblown dust has been suggested to enhance biological productivity and modulate the climate<sup>1–3</sup>. Yet, this process has never been quantified across the Southern Ocean and at annual timescales<sup>4,5</sup>. Here we combined 11 years of nitrate observations from autonomous biogeochemical ocean profiling floats with a Southern Hemisphere dust simulation to empirically derive the relationship between dust-iron deposition and annual net community production (ANCP) in the iron-limited Southern Ocean. Using this relationship, we determined the biological response to dust-iron in the pelagic perennially ice-free Southern Ocean at present and during the last glacial maximum (LGM). We estimate that dust-iron now supports  $33\% \pm 15\%$  of Southern Ocean ANCP. During the LGM, when dust deposition was 5–40-fold higher than today, the contribution of dust to Southern Ocean ANCP was much greater, estimated at  $64\% \pm 13\%$ . We provide quantitative evidence of basin-wide dust-iron fertilization of the Southern Ocean and the potential magnitude of its impact on glacial–interglacial timescales, supporting the idea of the important role of dust in the global carbon cycle and climate<sup>6–8</sup>.

Photosynthesizing primary producers (phytoplankton) inhabiting the sunlit ocean surface fix dissolved inorganic carbon and other nutrients, support the base of the marine food web and facilitate carbon export to depth<sup>9</sup>. This process, one of the factors regulating atmospheric carbon dioxide ( $\text{CO}_2$ ) concentrations and therefore climate, is termed the biological carbon pump<sup>10,11</sup>. Primary productivity in the Southern Ocean is seasonally limited by light and the micronutrient iron<sup>12–14</sup>. Consequently, the Southern Ocean's biological carbon pump does not operate at its maximum efficiency<sup>15</sup>. Changes in the supply of iron to the Southern Ocean, either through natural variability or deliberate human intervention, therefore have the potential to impact atmospheric  $\text{CO}_2$ . Thus, to understand the role of the Southern Ocean in the global carbon cycle it is critical to investigate the response of its ecosystems to iron addition.

Windblown mineral dust is enriched in iron (about 3.5 wt% (ref. 16)), allowing it to relieve iron stress in the Southern Ocean and thereby stimulate the biological carbon pump and export production<sup>6,8,17</sup>. The iron hypothesis<sup>1</sup> posits that increased dust fluxes to the Southern Ocean during glacial periods led to lower atmospheric  $\text{CO}_2$  through fertilization of Southern Ocean productivity. Although the iron hypothesis has been examined in a palaeo-oceanographic context<sup>3,18,19</sup> and tested in numerical models which simulate the biological response to dust-iron addition<sup>7,20,21</sup>, there are almost no observational constraints on the relationship between dust and ocean productivity. The response of Southern Ocean productivity to iron addition (not dust) has only been assessed through spatially and temporally restricted artificial<sup>22,23</sup> and

natural<sup>24</sup> iron fertilization experiments. None has quantified this process across the whole Southern Ocean and at annual timescales. Others<sup>4</sup> have attempted to quantify the basin-wide Southern Ocean biological response to dust. However, relying on shipboard measurements, they integrated productivity only over brief periods during the growing season<sup>25</sup> and neglected several important regions, most notably the South Atlantic downwind of Patagonia. It was further noted by ref. 5 that ref. 4 relied on dust-derived soluble iron fluxes from a model constrained for northern hemisphere conditions, with limited applicability in the Southern Ocean.

Here we combine *in situ* nitrate ( $\text{NO}_3^-$ ) concentrations, measured between 2012 and 2022 by biogeochemical Argo (BGC-Argo) floats (Fig. 1a), with a 2015–2019 Southern Hemisphere dust deposition simulation (ACCESS-AM2) (Fig. 1b) to quantify the dependence of present-day and glacial Southern Ocean productivity on dust-supplied iron. We calculated annual net community productivity (ANCP) in the mixed surface layer (0–50 m) and in the epipelagic zone (0–200 m) from the float-observed biological nitrate drawdown<sup>26</sup> in 50 dust regimes, ranging from low ( $0\text{--}0.2 \text{ mg m}^{-2} \text{ d}^{-1}$  annual mean dust flux) to high dust concentrations ( $4.7\text{--}12 \text{ mg m}^{-2} \text{ d}^{-1}$ ) (Fig. 2 and Extended Data Figs. 1 and 2). Observations in nitrate-deficient subtropical waters, the sea-ice zone and near the continental shelves were excluded from the climatologies (masks shown in Fig. 1a), ensuring that the nitrate-derived productivity estimates reflect the annual biological response to dust-iron rather than other iron sources. Relating regime-averaged ANCP to dust deposition showed a statistically significant basin-wide relationship

<sup>1</sup>Institute for Marine and Antarctic Studies (IMAS), University of Tasmania, Hobart, Tasmania, Australia. <sup>2</sup>Australian Research Council Centre of Excellence for Climate Extremes (CLEX), University of Tasmania, Hobart, Tasmania, Australia. <sup>3</sup>Australian Research Council Centre for Excellence in Antarctic Science (ACEAS), University of Tasmania, Hobart, Tasmania, Australia. <sup>4</sup>Australian Antarctic Program Partnership (AAPP), University of Tasmania, Hobart, Tasmania, Australia. <sup>5</sup>Environment, CSIRO, Hobart, Tasmania, Australia. ✉e-mail: jakob.weis@utas.edu.au

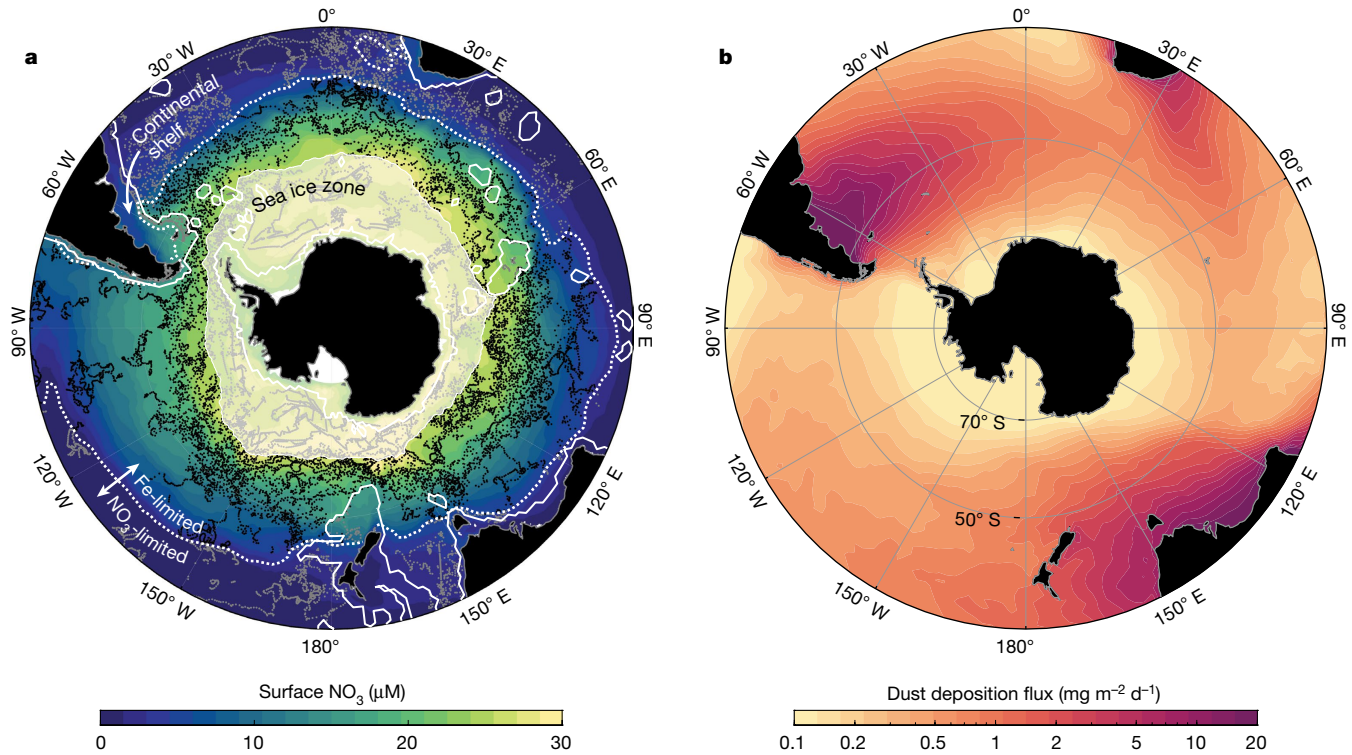


**Fig. 1 | Southern Ocean surface nitrate and dust deposition.** **a**, Annual mean surface nitrate ( $\text{NO}_3^-$ ) concentrations (B-SOSE, 2013–2021 climatology) and BGC-Argo nitrate profile locations from 2012 to 2022. Three regional masks were applied to restrict the study to regions in which a pronounced biological response to dust-iron fertilization is expected: a nitrate limitation mask (dotted white line;  $\text{NO}_3^-$ :chlorophyll less than  $20 \text{ mol g}^{-1}$ ), a sea-ice mask (light

shade; September sea-ice concentration more than 15%) and a shallow bathymetry mask (solid white line; water depth less than 2,000 m). Excluded float observations in masked regions are shown in grey. **b**, Simulated seasonal mean dust deposition fluxes (ACCESS-AM2, 2015–2019 September–March climatology) (Methods).

between productivity and dust-iron addition applicable to the pelagic and perennially ice-free Southern Ocean. Applying this relationship to present-day and last glacial maximum (LGM) (21 thousand years ago (ka); ECHAM6 (ref. 27)) dust simulations further allowed us to calculate Southern Ocean-wide ANCP maps and estimate the contribution of dust to Southern Ocean productivity and its glacial–interglacial variability.

### Relationship between dust and productivity

The Southern Ocean nitrate inventory follows a seasonal cycle driven by biological activity and mixing (Fig. 2 and Extended Data Figs. 2 and 3). In austral spring and summer, surface nitrate is depleted by phytoplankton as mixed layers are generally shoaling and nitrate entrainment is negligible<sup>28</sup>. During the unproductive autumn and winter season, nitrate is replenished again through the entrainment of nutrient-rich subsurface waters, whereas nitrate consumption by phytoplankton is light limited<sup>29</sup>. The productive period, defined here between winter maximum and summer minimum surface nitrate concentrations, starts in August or September and ends between January and March (Extended Data Fig. 3)<sup>28</sup>.

We calculated the annual surface nitrate drawdown ( $\Delta\text{NO}_3^-$ ,  $\text{mmol m}^{-2} \text{yr}^{-1}$ ), defined as the depth-integrated nitrate drawdown throughout the productive period and determined ANCP ( $\text{mol C m}^{-2} \text{yr}^{-1}$ ) by applying a Redfield C:N ratio of 106:16 (ref. 30). This method assumes negligible growth in autumn and winter, negligible horizontal and vertical advection<sup>26,31</sup> and a regionally constant C:N ratio under nitrate-replete conditions<sup>32</sup>. Given the inherent spatial heterogeneity of the Southern Ocean, these assumptions might not hold universally. However, considering the extensive geographical span of the dust regimes, the resultant biases are presumably minimal. We integrated  $\Delta\text{NO}_3^-$  and ANCP

to 50 m ( $\text{ANCP}_{50\text{m}}$ ), the median January mixed layer depth derived from float conductivity, temperature and depth (CTD) data and to 200 m ( $\text{ANCP}_{200\text{m}}$ ), consistent with previous studies<sup>26,31</sup>. The mixed layer is commonly used as a reference for productivity estimates following deliberate ocean iron fertilization studies<sup>2,33</sup>. During most of the productive period, the mixed layer is shallower than the euphotic zone<sup>34</sup> and the biological response to dust-iron addition is not limited by light.

We related dust-regime-averaged  $\text{ANCP}_{50\text{m}}$  and  $\text{ANCP}_{200\text{m}}$  to mean dust deposition fluxes during the productive period (Fig. 3), showing a pronounced basin-wide biological response to dust-iron addition. In regions receiving less than  $7 \text{ mg dust m}^{-2} \text{d}^{-1}$ , presently covering about 98% of the pelagic ice-free Southern Ocean south of 30° S, both  $\text{ANCP}_{50\text{m}}$  and  $\text{ANCP}_{200\text{m}}$  increase linearly with dust deposition. We used two statistically significant linear regression models quantifying the ANCP–dust relationship above 50 m and above 200 m (Fig. 3). The regression slopes represent the biological response to dust-iron addition and the y intercepts represent productivity in the absence of dust (hereafter ‘background ANCP’). The increase of both slope and intercept from the 50-m-regression to the 200-m-regression therefore implies a more or less constant percentage contribution of dust to productivity throughout the epipelagic zone. The marked increase in variability of  $\text{ANCP}_{200\text{m}}$  is attributed to a stronger influence of subsurface processes on productivity at depth compared to the predominantly dust-driven productivity trend observed above 50 m.

The biological response to dust in regions exceeding  $7 \text{ mg dust m}^{-2} \text{d}^{-1}$ , covering about 2% of the pelagic ice-free Southern Ocean, differs distinctly from the response in low- and medium-dust regimes. Here,  $\text{ANCP}_{50\text{m}}$  reaches a plateau whereas  $\text{ANCP}_{200\text{m}}$  declines sharply, approaching  $\text{ANCP}_{50\text{m}}$  concentrations as dust deposition increases. This implies saturation of dust-supported productivity and provides

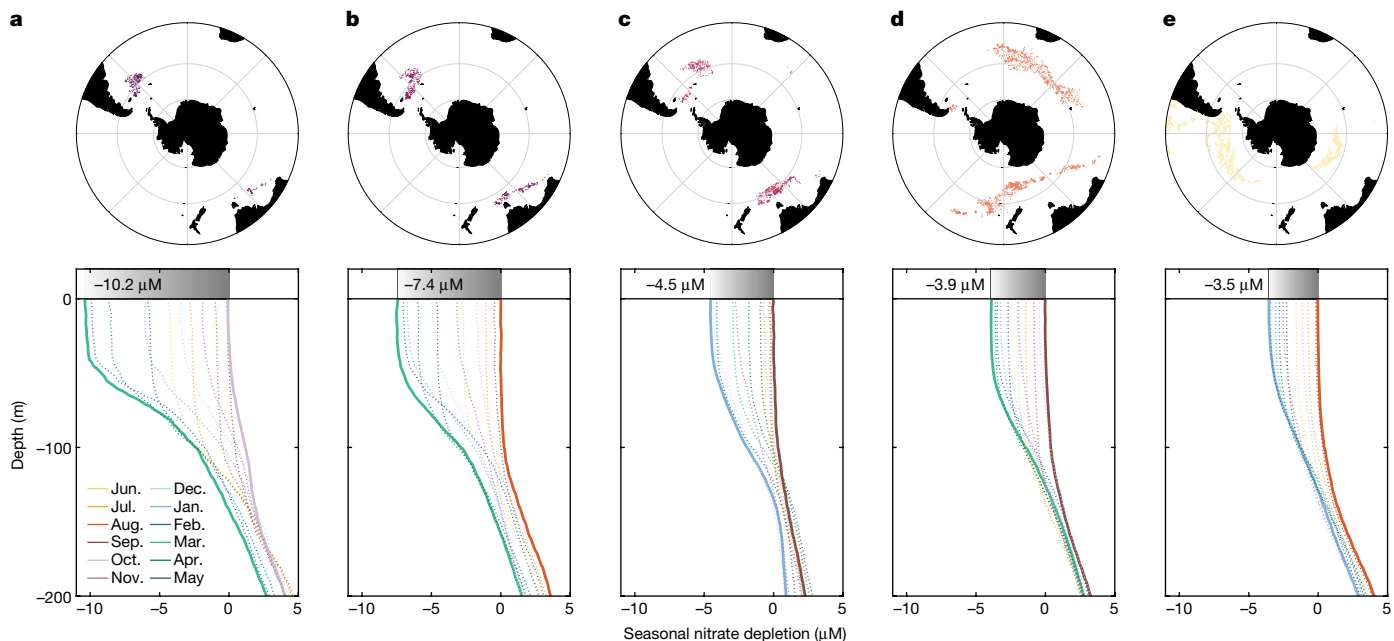


**Fig. 2 | Seasonal variability of nitrate in the epipelagic zone.** a–e, Monthly depth-resolved nitrate climatologies in the upper 200 m in five dust regimes, with dust deposition limits of  $3.8\text{--}7.5 \text{ mg m}^{-2} \text{ d}^{-1}$  (a),  $2.7\text{--}5.2 \text{ mg m}^{-2} \text{ d}^{-1}$  (b),  $1.4\text{--}2.6 \text{ mg m}^{-2} \text{ d}^{-1}$  (c),  $0.4\text{--}0.7 \text{ mg m}^{-2} \text{ d}^{-1}$  (d) and  $0\text{--}0.2 \text{ mg m}^{-2} \text{ d}^{-1}$  (e). Nitrate climatologies were calculated from BGC-Argo nitrate profiles, shown on the maps, measured between 2012 and 2022 in each regime, grouped by month. Plotted on the x axis is the difference in nitrate concentration relative to the

winter surface nitrate maximum, illustrating the seasonal nitrate depletion in the epipelagic zone. The horizontal grey bar above the nitrate climatologies indicates the 50-m-averaged seasonal nitrate difference between the winter maximum to the summer minimum (solid profiles). Regime maps and nitrate climatologies of the 50 regimes defined in this study are shown in Extended Data Figs. 1 and 2.

a compelling perspective on the potential physical constraint of natural and deliberate large-scale ocean iron fertilization. Potential dust-related limiting factors include iron-scavenging due to high biogenic and mineral particle concentrations or iron-binding ligand saturation<sup>35,36</sup> and light limitation due to self-shading<sup>37</sup>. The latter could further explain the more pronounced reduction of productivity at depth compared to the surface. Nitrate is unlikely to be a limiting factor because we excluded nitrate-deficient regions.

To assess the validity of the ANCP–dust relationship, we derived cellular iron requirements ( $\mu\text{mol Fe (mol C)}^{-1}$ ) (Extended Data Fig. 4) from the 200-m-integrated daily net community production ( $\text{mol C m}^{-2} \text{ d}^{-1}$ ,  $\text{ANCP}_{200\text{m}}$  divided by the productive period duration) and bioavailable iron fluxes ( $\mu\text{mol Fe m}^{-2} \text{ d}^{-1}$ ). Bioavailable iron was derived from dust assuming 3.5 wt% dust-iron content<sup>16</sup> and a soluble iron fraction ranging from 5% to 15% (ref. 38). We estimate Southern Ocean basin-averaged Fe:C ratios ranging from 5 to 15  $\mu\text{mol mol}^{-1}$ , which are in very good agreement with modelled (3–16  $\mu\text{mol mol}^{-1}$ )<sup>39</sup> and in situ (3.92  $\mu\text{mol mol}^{-1}$ , South Pacific transect)<sup>40</sup> Fe:C ratios in Southern Ocean phytoplankton. This analysis confirms that the observed increase in carbon fixation can be supported entirely by dust-iron and thereby implies a limited impact from alternative atmospheric iron sources, such as pyrogenic iron deposition<sup>41</sup>. Because of the episodic nature of pyrogenic iron fertilization events, such as the 2019–2020 Australian wildfires<sup>42,43</sup> and their differing source regions from those of dust, their contribution to Southern Ocean productivity is probably represented in the background and variability of our ANCP estimates and does not bias the relationship with dust.

To further examine whether the observed increase of productivity with dust is affected by alternative drivers of productivity, namely, mixing, temperature and insolation, we calculated individual and multiple linear regressions between ANCP and mixed layer changes, temperature and latitude (Extended Data Fig. 5 and Methods). This analysis found no significant influence of these parameters on the

ANCP–dust relationship. A quantitative evaluation of temperature limitation factors, commonly used in phytoplankton ecosystem models to parameterize growth limitation at low temperatures, further suggests that temperature differences between dust regimes alone could only explain a minor fraction of the observed increase in ANCP (Extended Data Fig. 5 and Methods). Last, iron supply from upwelling during the productive season is negligible because of the exclusion of the sea-ice zone where subsurface iron supply is potentially more important<sup>29</sup> and because the spring/summer ferricline in the study region consistently remains well below 50 m and mostly below 200 m (ref. 29). From this we conclude that the influence of temperature, light, mixing and upwelling on productivity is either negligible or reflected in the background and the variability of our ANCP estimates.

## Dust contribution to Southern Ocean productivity

On the basis of the evidence presented, we deduce that iron from dust is indeed the primary driver of the relationship between ANCP and dust in the iron-deficient Southern Ocean and that this relationship is well explained by our regressions. This means we can apply the regressions to dust deposition fluxes mapped in Fig. 1b to compute  $\text{ANCP}_{50\text{m}}$  (Fig. 4a) and  $\text{ANCP}_{200\text{m}}$  maps (Extended Data Fig. 6). To account for growth limitation at high dust due to iron-scavenging and self-shading, we assume constant  $\text{ANCP}_{50\text{m}}$  in regions exceeding  $7 \text{ mg dust m}^{-2} \text{ d}^{-1}$ , as indicated by the dashed line in Fig. 3. The same regions were omitted in the  $\text{ANCP}_{200\text{m}}$  calculation because of the uncertainty associated with modelling the observed decline in subsurface productivity with dust. We retained the sea-ice and shelf masks used earlier. However, we abandoned the nitrate limitation mask and simulated the midseason onset of nitrate limitation in nitrate-deficient regions by applying an upper ANCP limit based on the winter surface nitrate inventory (Extended Data Fig. 7). High-dust-impacted and nitrate-limited regions are indicated in Fig. 4. Regions accounted for in the basin-integrated

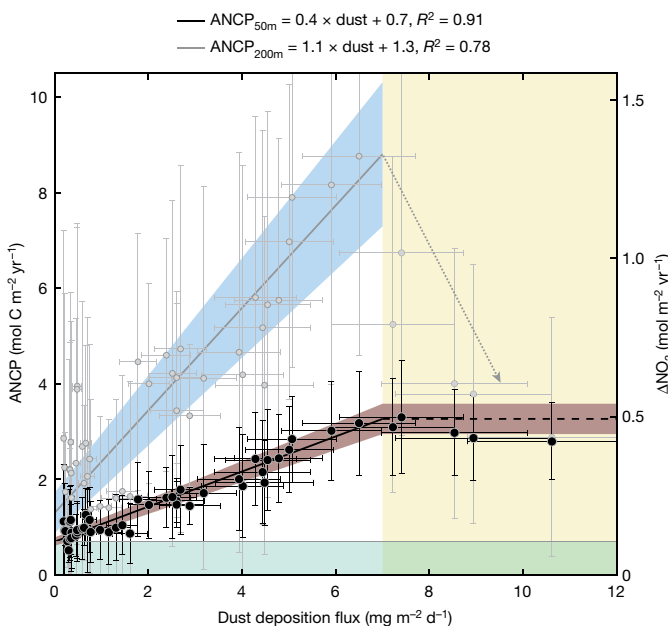


**Fig. 3 | Annual surface nitrate drawdown ( $\Delta\text{NO}_3$ ) and ANCP as a function of dust deposition.**  $\Delta\text{NO}_3$  and ANCP (derived from  $\Delta\text{NO}_3$  using a C:N Redfield ratio of 106:16)<sup>30</sup> integrated to 50 m (black markers) and 200 m (grey markers) and regressed against dust deposition in 50 distinct dust regimes (Extended Data Figs. 1 and 2). Vertical error bars represent the regional variability of ANCP (Methods) and horizontal error bars the standard deviation ( $\pm 1\sigma$ ) of the regime-averaged dust deposition fluxes. Below 7 mg dust  $\text{m}^{-2} \text{d}^{-1}$ , both ANCP<sub>50m</sub> and ANCP<sub>200m</sub> show statistically significant linear relationships with dust ( $P < 10^{-15}$ , solid lines with  $\pm 2\sigma$  uncertainty bounds, shown as red and blue shaded areas). Above 7 mg dust  $\text{m}^{-2} \text{d}^{-1}$ , indicated by the yellow-shaded area, ANCP<sub>50m</sub> is limited by iron-scavenging and self-shading and assumed to be constant (dashed line) in the model used to derive ANCP<sub>50m</sub> maps. Owing to the uncertainty of the ANCP<sub>200m</sub> decline at high dust (dotted arrow), these regions were excluded from the ANCP<sub>200m</sub> versus dust model. The green-shaded area indicates the background ANCP<sub>50m</sub> value (estimated at the y intercept) used for the calculation of dust contributions (Fig. 4b,d).

estimates, namely the pelagic ice-free Southern Ocean south of 30° S, will hereafter be referred to as ‘Southern Ocean’.

Across most of the Southern Ocean, both ANCP<sub>50m</sub> and ANCP<sub>200m</sub> follow the spatial distribution of dust from which they are derived. At low latitudes (30°–40° S), simulated nitrate limitation produces Southern Ocean minimum ANCP concentrations consistent with oligotrophic conditions in the subtropical oceans. Basin-integrated ANCP<sub>50m</sub> and ANCP<sub>200m</sub> amount to a Southern Ocean annual production of  $0.91 \pm 0.10$  and  $2.02 \pm 0.43 \text{ PgC}$ , respectively. Note that the ANCP<sub>200m</sub> estimate was integrated over a slightly smaller area because of the exclusion of high-dust regions (see the respective figure captions). Averaged across 5°-latitude bands, ANCP<sub>200m</sub> is in very good agreement, both in magnitude and meridional trend, with corresponding literature values<sup>26,31</sup> (Extended Data Fig. 6). The percentage contribution of dust-iron fertilization to Southern Ocean ANCP (Fig. 4b), defined as the difference between ANCP and the background, divided by ANCP, ranges from zero, in regions farthest from dust sources and in the oligotrophic subtropical oceans, to about 70% directly downwind of the dust sources. Averaged across the basin, we estimate that dust presently supports  $33\% \pm 15\%$  of Southern Ocean ANCP<sub>50m</sub>. Although we refrain from presenting mapped ANCP<sub>200m</sub> dust contributions because of their increased uncertainty, the basin-averaged dust contribution in the upper 200 m ( $42\% \pm 30\%$ ) is consistent with the contribution in the upper 50 m, which substantiates our previous assertion that the biological response to dust is relatively constant throughout the epipelagic zone.

The ANCP and dust contribution maps offer valuable insights into the Southern Ocean carbon sink. The carbon sink follows a distinct meridional pattern with maximum net ocean carbon uptake occurring in highly productive midlatitudes<sup>44</sup>. This trend has been attributed in part to enhanced biological carbon export<sup>32</sup> and coincides well with the strongly dust-impacted midlatitudes (Fig. 4 and Extended Data Fig. 6). The apparent link between dust-fertilization and the strength of the biological carbon pump underscores the importance of dust-iron for the potential of the Southern Ocean to sequester anthropogenic carbon.

### Implications for the glacial Southern Ocean

Dust deposition during the LGM, which was 5–40 times higher than today<sup>27</sup>, is believed to have stimulated Southern Ocean carbon export and contributed to reduced atmospheric CO<sub>2</sub> concentrations and cooler mean global temperatures<sup>3,6,18,19</sup>. To better constrain the magnitude of increased glacial productivity, we computed LGM ANCP<sub>50m</sub> and dust contribution maps (Fig. 4c,d) on the basis of simulated LGM dust fluxes (Extended Data Fig. 8) following the same approach used to calculate present-day ANCP maps. We did not calculate ANCP<sub>200m</sub> maps for the LGM because of the uncertainty of ANCP<sub>200m</sub> at more than 7 mg dust  $\text{m}^{-2} \text{d}^{-1}$ , covering about 22% of the glacial Southern Ocean. Note that we do not account for several factors that are known to influence Southern Ocean productivity on glacial–interglacial timescales, some of which would result in lower ANCP during glacial periods (for example, larger sea-ice extent, colder sea surface temperatures and reduced upwelling in the Antarctic zone<sup>45</sup>), whereas others would result in higher ANCP (for example, increased dust-iron bioavailability<sup>46</sup>).

We estimate that, under increased glacial dust loads, ANCP<sub>50m</sub> ( $1.71 \pm 0.17 \text{ PgC yr}^{-1}$ ) exceeded present-day productivity concentrations by 90%. Assuming present-day background ANCP, basin-averaged dust contributions are estimated to have increased to  $64 \pm 13\%$  during the LGM, supporting an extra 31% of Southern Ocean productivity compared to the present-day. The dust-model-derived glacial–interglacial change in productivity was independently confirmed in each of the three Southern Ocean basins by comparison with subantarctic export production fluxes derived from sedimentary records (Extended Data Table 1). This comparison demonstrates that the dust–ANCP regression model produces reasonable subantarctic productivity estimates for the LGM, despite the simplifying assumptions. However, the proxy data also indicate that in the Antarctic zone, reduced subsurface nutrient supply led to reduced productivity and stronger nitrate depletion<sup>45</sup>. In our calculations, we assume that productivity supported by subsurface nutrients is reflected in the background ANCP. Consequently, reducing subsurface nutrient supply would primarily lower the background but not the dust-supported productivity and thus lead to an increase in the dust contribution. These effects are not accounted for in our LGM estimates in the Antarctic, which assume present-day nutrient supply and therefore presumably overestimate ANCP and underestimate the dust contribution (Fig. 4c,d).

The glacial–interglacial difference in dust-supported productivity is most pronounced in remote regions; in near-source regions, dust-induced nitrate limitation, iron-scavenging and self-shading may have hindered a strong increase in productivity. These regions are estimated to have doubled in area from 17 million km<sup>2</sup> at present to 25 million km<sup>2</sup> during the LGM, affecting 22% and 45% of the pelagic ice-free Southern Ocean south of 30° S, respectively (Extended Data Fig. 9), underscoring the far-reaching impact dust had on glacial Southern Ocean productivity and still has today. From this also follows that a considerable part of the present-day Southern Ocean is either reaching or nearing nitrate depletion on an annual basis and thus may have a limited capacity to be fertilized through deliberate or natural iron addition alone.

The basin-scale natural iron fertilization study presented here was largely enabled by the international BGC-Argo programme and the

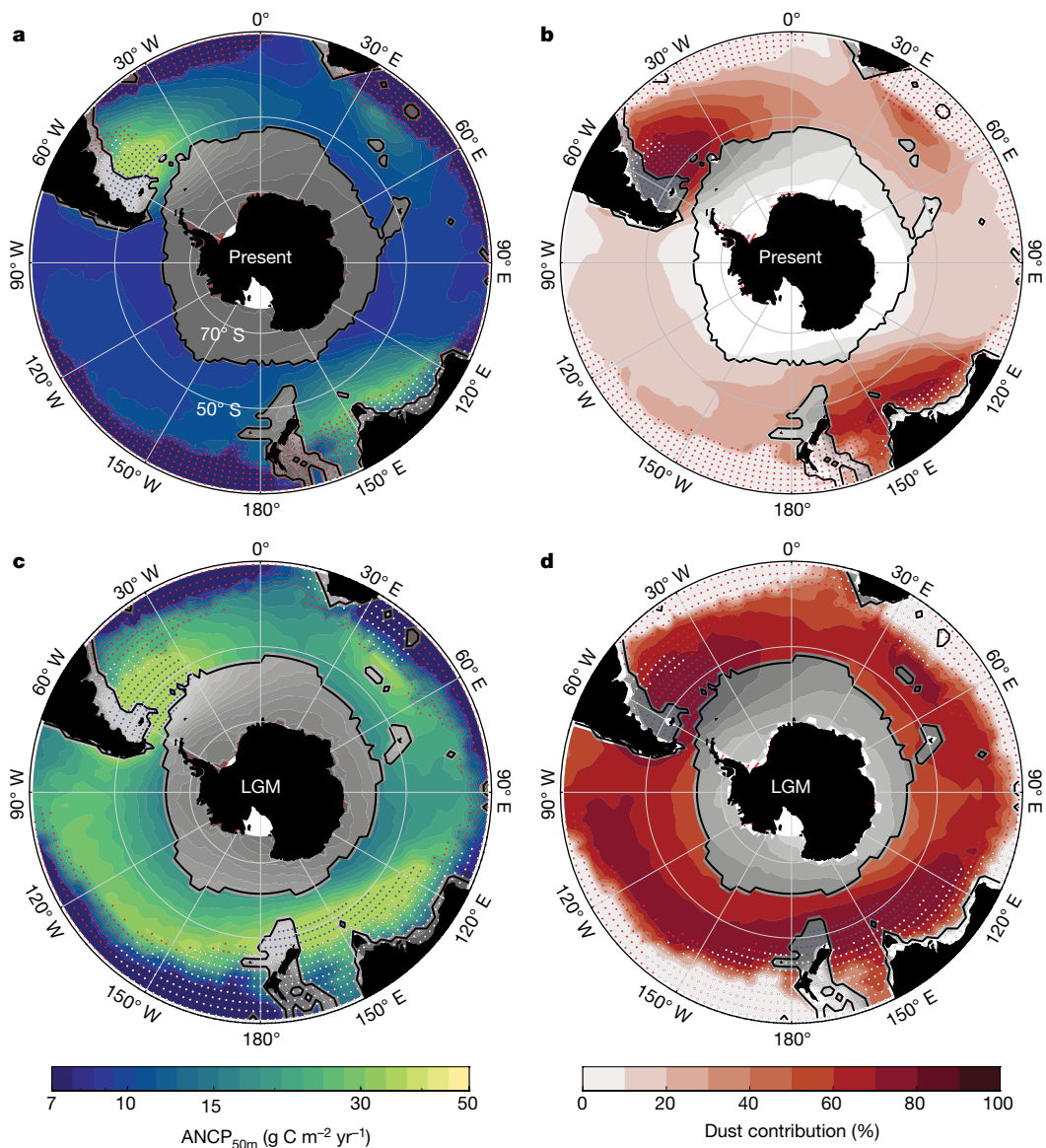


**Fig. 4 | ANCP<sub>50m</sub> derived from present-day and LGM dust deposition.** **a–d**, Present-day (**a**, **b**) and LGM (**c**, **d**) ANCP<sub>50m</sub> (**a**, **c**) and percentage dust contribution maps (**b**, **d**) derived from ACCESS-AM2 and ECHAM6 (ref. 27) simulated dust deposition fluxes using the ANCP<sub>50m</sub> versus dust model (black lines in Fig. 3). Dots indicate regions where productivity is affected by high dust

loads leading to iron-scavenging and self-shading (blue, more than 7 mg dust m<sup>-2</sup> d<sup>-1</sup>), by nitrate limitation (red) or both (white). Regions accounted for in the basin-integrated ANCP and dust contribution estimates, highlighted in colour, exclude the sea-ice zone and shelf regions and cover an area of 78 million km<sup>2</sup>.

SOCCOM project. The global BGC-Argo array provides an indispensable source of information for ocean biological studies through continuous ocean-covering biogeochemical observations, particularly in regions and seasons that are not commonly targeted during field campaigns. Although some uncertainties remain, these observations show that the vital function of dust as a stimulant of the Southern Ocean carbon pump is not limited to glacial periods but remains considerable even under moderate dust loads in the present-day oceans. This emphasizes the need for accurate representation of dust-supplied iron and its effect on primary productivity and nutrient cycles in biogeochemical ocean models<sup>47</sup>, which is imperative for improving our understanding of modern-day climate variability.

## Online content

Any methods, additional references, Nature Portfolio reporting summaries, source data, extended data, supplementary information,

acknowledgements, peer review information; details of author contributions and competing interests; and statements of data and code availability are available at <https://doi.org/10.1038/s41586-024-07366-4>.

1. Martin, J. H. Glacial-interglacial CO<sub>2</sub> change: the iron hypothesis. *Paleoceanography* **5**, 1–13 (1990).
2. Boyd, P. W. et al. A mesoscale phytoplankton bloom in the polar Southern Ocean stimulated by iron fertilization. *Nature* **407**, 695–702 (2000).
3. Martinez-Garcia, A. et al. Iron fertilization of the subantarctic ocean during the last ice age. *Science* **343**, 1347–1350 (2014).
4. Cassar, N. et al. The Southern Ocean biological response to aeolian iron deposition. *Science* **317**, 1067–1070 (2007).
5. Boyd, P. W. & Mackie, D. Comment on the Southern Ocean biological response to aeolian iron deposition. *Science* **319**, 159–159 (2008).
6. Jickells, T. D. et al. Global iron connections between desert dust, ocean biogeochemistry and climate. *Science* **308**, 67–71 (2005).
7. Lambert, F. et al. Dust fluxes and iron fertilization in Holocene and Last Glacial Maximum climates. *Geophys. Res. Lett.* **42**, 6014–6023 (2015).
8. Emerson, D. Biogenic iron dust: a novel approach to ocean iron fertilization as a means of large scale removal of carbon dioxide from the atmosphere. *Front. Mar. Sci.* **6**, 22 (2019).

9. Sarmiento, J. L. & Gruber, N. in *Ocean Biogeochemical Dynamics* Ch. 8 (Princeton Univ. Press, 2006).
10. Boyd, P. W., Claustre, H., Levy, M., Siegel, D. A. & Weber, T. Multi-faceted particle pumps drive carbon sequestration in the ocean. *Nature* **568**, 327–335 (2019).
11. Buesseler, K. O. et al. Revisiting carbon flux through the ocean's twilight zone. *Science* **316**, 567–570 (2007).
12. Mitchell, B. G., Brody, E. A., Holmhansen, O., McClain, C. & Bishop, J. Light limitation of phytoplankton biomass and macronutrient utilization in the Southern Ocean. *Limnol. Oceanogr.* **36**, 1662–1677 (1991).
13. Martin, J. H., Gordon, R. M. & Fitzwater, S. E. Iron in Antarctic waters. *Nature* **345**, 156–158 (1990).
14. Boyd, P. W. Environmental factors controlling phytoplankton processes in the Southern Ocean. *J. Phycol.* **38**, 844–861 (2002).
15. DeVries, T., Primeau, F. & Deutsch, C. The sequestration efficiency of the biological pump. *Geophys. Res. Lett.* <https://doi.org/10.1029/2012GL051963> (2012).
16. Mahowald, N. M. et al. Atmospheric global dust cycle and iron inputs to the ocean. *Glob. Biogeochem. Cy.* <https://doi.org/10.1029/2004GB002402> (2005).
17. Hamilton, D. S. et al. Earth, wind, fire and pollution: aerosol nutrient sources and impacts on ocean biogeochemistry. *Annu. Rev. Mar. Sci.* **14**, 303–330 (2022).
18. Lamy, F. et al. Increased dust deposition in the Pacific Southern Ocean during glacial periods. *Science* **343**, 403–407 (2014).
19. Röhlisberger, R. et al. Ice core evidence for the extent of past atmospheric CO<sub>2</sub> change due to iron fertilisation. *Geophys. Res. Lett.* <https://doi.org/10.1029/2004GL020338> (2004).
20. Muglia, J., Somes, C. J., Nickelsen, L. & Schmittner, A. Combined effects of atmospheric and seafloor iron fluxes to the glacial ocean. *Paleoceanography* **32**, 1204–1218 (2017).
21. Saini, H. et al. Southern Ocean ecosystem response to Last Glacial Maximum boundary conditions. *Paleoceanogr. Paleoclimatol.* **36**, e2020PA004075 (2021).
22. Boyd, P. W. et al. Mesoscale iron enrichment experiments 1993–2005: synthesis and future directions. *Science* **315**, 612–617 (2007).
23. Yoon, J. E. et al. Reviews and syntheses: ocean iron fertilization experiments—past, present and future looking to a future Korean iron fertilization experiment in the Southern Ocean (KIFES) project. *Biogeosciences* **15**, 5847–5889 (2018).
24. Blain, S., Sarthou, G. & Laan, P. Distribution of dissolved iron during the natural iron-fertilization experiment KEOPS (Kerguelen Plateau, Southern Ocean). *Deep-Sea Res. II* **55**, 594–605 (2008).
25. Kaiser, J., Reuer, M. K., Barnett, B. & Bender, M. L. Marine productivity estimates from continuous O<sub>2</sub>/Ar ratio measurements by membrane inlet mass spectrometry. *Geophys. Res. Lett.* <https://doi.org/10.1029/2005GL023459> (2005).
26. Johnson, K. S., Plant, J. N., Dunne, J. P., Talley, L. D. & Sarmiento, J. L. Annual nitrate drawdown observed by SOCCOM profiling floats and the relationship to annual net community production. *J. Geophys. Res. Oceans* **122**, 6668–6683 (2017).
27. Krätschmer, S. et al. Simulating glacial dust changes in the Southern Hemisphere using ECHAM6.3-HAM2.3. *Clim. Past* **18**, 67–87 (2022).
28. Arrigo, K. R., van Dijken, G. L. & Bushinsky, S. Primary production in the Southern Ocean, 1997–2006. *J. Geophys. Res. Oceans* <https://doi.org/10.1029/2007JC004551> (2008).
29. Tagliabue, A. et al. Surface-water iron supplies in the Southern Ocean sustained by deep winter mixing. *Nat Geosci.* **7**, 314–320 (2014).
30. Redfield, A. C. The biological control of chemical factors in the environment. *Am. Sci.* **46**, 205–221 (1958).
31. Arteaga, L. A., Pahlow, M., Bushinsky, S. M. & Sarmiento, J. L. Nutrient controls on export production in the Southern Ocean. *Glob. Biogeochem. Cy.* **33**, 942–956 (2019).
32. Huang, Y., Fassbender, A. J. & Bushinsky, S. M. Biogenic carbon pool production maintains the Southern Ocean carbon sink. *Proc. Natl. Acad. Sci. USA* **120**, e2217909120 (2023).
33. Hiscock, W. T. & Miller, F. J. Nutrient and carbon parameters during the Southern Ocean iron experiment (SOFeX). *Deep-Sea Res. I* **52**, 2086–2108 (2005).
34. Su, J. Y., Schallenberg, C., Rohr, T., Strutton, P. G. & Phillips, H. E. New estimates of Southern Ocean annual net community production revealed by BGC-Argo floats. *Geophys. Res. Lett.* **49**, e2021GL097372 (2022).
35. Schallenberg, C., Ross, A. R. S., Davidson, A. B., Stewart, G. M. & Cullen, J. T. Temporal variability of dissolved iron species in the mesopelagic zone at Ocean Station PAPA. *J. Mar. Syst.* **172**, 128–136 (2017).
36. Moore, J. K. & Braucher, O. Sedimentary and mineral dust sources of dissolved iron to the world ocean. *Biogeosciences* **5**, 631–656 (2008).
37. Twelves, A. G., Goldberg, D. N., Henley, S. F., Mazloff, M. R. & Jones, D. C. Self-shading and meltwater spreading control the transition from light to iron limitation in an Antarctic coastal polynya. *J. Geophys. Res. Oceans* **126**, e2020JC016636 (2021).
38. Perron, M. M. G. et al. Origin, transport and deposition of aerosol iron to Australian coastal waters. *Atmos. Environ.* **228**, 117432 (2020).
39. Wiseman, N. A., Moore, J. K., Twining, B. S., Hamilton, D. S. & Mahowald, N. M. Acclimation of phytoplankton Fe:C ratios dampens the biogeochemical response to varying atmospheric deposition of soluble iron. *Glob. Biogeochem. Cy.* **37**, e2022GB007491 (2023).
40. Tagliabue, A. et al. The interplay between regeneration and scavenging fluxes drives ocean iron cycling. *Nat. Commun.* **10**, 4960 (2019).
41. Ito, A. et al. Pyrogenic iron: the missing link to high iron solubility in aerosols. *Sci. Adv.* <https://doi.org/10.1126/sciadv.aau7671> (2019).
42. Tang, W. Y. et al. Widespread phytoplankton blooms triggered by 2019–2020 Australian wildfires. *Nature* **597**, 370–375 (2021).
43. Weis, J. et al. Southern Ocean phytoplankton stimulated by wildfire emissions and sustained by iron recycling. *Geophys. Res. Lett.* **49**, e2021GL097538 (2022).
44. Henley, S. F. et al. Changing biogeochemistry of the Southern Ocean and its ecosystem implications. *Front. Mar. Sci.* <https://doi.org/10.3389/fmars.2020.00581> (2020).
45. Sigman, D. M. et al. The Southern Ocean during the ice ages: a review of the Antarctic surface isolation hypothesis, with comparison to the North Pacific. *Quat. Sci. Rev.* **254**, 106732 (2021).
46. Shoenfelt, E. M., Winckler, G., Lamy, F., Anderson, R. F. & Bostick, B. C. Highly bioavailable dust-borne iron delivered to the Southern Ocean during glacial periods. *Proc. Natl. Acad. Sci. USA* **115**, 11180–11185 (2018).
47. Tagliabue, A. et al. How well do global ocean biogeochemistry models simulate dissolved iron distributions? *Glob. Biogeochem. Cy.* **30**, 149–174 (2016).

**Publisher's note** Springer Nature remains neutral with regard to jurisdictional claims in published maps and institutional affiliations.

Springer Nature or its licensor (e.g. a society or other partner) holds exclusive rights to this article under a publishing agreement with the author(s) or other rightsholder(s); author self-archiving of the accepted manuscript version of this article is solely governed by the terms of such publishing agreement and applicable law.

© The Author(s), under exclusive licence to Springer Nature Limited 2024

## Methods

### BGC-Argo data

Nitrate ( $\text{NO}_3^-$ ) data were collected by in situ profiling floats, mostly deployed under the Southern Ocean Carbon and Climate Observations and Modeling project (SOCCOM), part of the international BGC-Argo effort. Depth-resolved nitrate observations were obtained from 252 BGC-Argo floats south of 30°S between January 2012 and December 2022. In situ nitrate concentrations ( $\mu\text{M}$ ) were measured by two types of nitrate spectrophotometers: the In Situ Ultraviolet Spectrophotometer (ISUS, 200 floats) manufactured by the Monterey Bay Aquarium Research Institute (MBARI)<sup>48</sup> and the Submersible Ultraviolet Nitrate Analyzer (SUNA, v.1 and 2, 52 floats) manufactured by Sea-Bird Scientific<sup>49</sup>. Both sensors allow the calculation of the nitrate concentration from the absorption spectrum of ultraviolet light in the wavelength range from 217 to 240 nm corrected for the absorption by seawater, bromide and other sea salts<sup>50</sup>.

BGC-Argo data products were downloaded from the Institut Français de Recherche pour l'Exploitation de la Mer (IFREMER) and the US Global Ocean Data Assimilation Experiment (USGODAE) Argo Global Data Assembly Centers (GDAC) using the BGC-Argo-Mat toolbox for MATLAB<sup>51</sup>. These data were collected and made freely available by the International Argo Program and the national programmes that contribute to it (<https://argo.ucsd.edu> and <https://www.ocean-ops.org>).

Raw nitrate measurements are subject to temporal drift and need to be adjusted for potential offsets<sup>52</sup>. Initial quality control (QC) and corrections of the float data used in this analysis were performed at three different DACs: NOAA AOML in the United States, IFREMER in France and CSIRO in Australia. We used only corrected nitrate data (adjusted or delayed-mode) in the analysis. Float observations were filtered for good data with reference to Argo quality control flags assigned at the respective DACs (1, 2, 5, 8; [http://www.cmar.csiro.au/argo/dmqc/user\\_doc/QC\\_flags.html](http://www.cmar.csiro.au/argo/dmqc/user_doc/QC_flags.html)). Nitrate profiles with extreme outliers (nitrate range more than 50  $\mu\text{M}$ ) and lack of surface observations (no usable data above 50 m) were excluded from the analysis. Where nitrate profiles contained negative values, the entire profile was offset by the most negative value.

### Dust deposition models

The 2015–2019 daily dust deposition fluxes ( $1.25^\circ \times 1.875^\circ$  spatial resolution, daily resolved) (Fig. 1b) were obtained from the Australian Community Climate and Earth-System Simulator Atmosphere Model (ACCESS-AM2), which is an atmosphere-only version of the Coupled Model (ACCESS-CM2)<sup>53</sup>, run in an Atmospheric Model Intercomparison Project (AMIP) configuration. The specific model setup is described in ref. 54. ACCESS-AM2 includes a globally resolved modal aerosol scheme, has been nudged to ERA5 to reflect reality and uses the CSIRO Atmosphere Biosphere Land Exchange model (CABLE-2.5)<sup>53</sup>. Dust is represented in ACCESS-AM2 by the binned Woodward<sup>55</sup> scheme, which is separate to the aerosol scheme. It provides wet and dry dust deposition binned in six size classes (0.03–31.6  $\mu\text{m}$ ). We note that there is some uncertainty in using the Woodward scheme with CABLE, as detailed model tuning with respect to the CABLE land surface has not been performed. However, ACCESS-AM2 provided the most realistic dust fluxes when compared to other products, including MERRA2. Total present-day dust fluxes analysed in this study were summed across all size classes and deposition types. Outputs are publicly available<sup>56</sup>.

Dust deposition fluxes during the LGM (21 ka,  $1.875^\circ \times 1.875^\circ$ , annual mean) (Extended Data Fig. 8a) were obtained from the Atmosphere Model ECHAM6 (ref. 57), which is being developed as part of the Max Planck Institute Earth System Model (MPI-ESM). ECHAM6 is coupled with the Hamburg Aerosol Model (HAM2.3)<sup>58</sup>, simulating wet and dry dust deposition and atmospheric sedimentation binned in 192 size classes (0.2–1,300  $\mu\text{m}$ ). The specific model setup is described in ref. 27 and outputs (summed across all size classes and deposition types) were provided to us on request. The ECHAM6-HAMMOZ model code and

all required input data are maintained and made available at <https://redmine.hammoz.ethz.ch> (ref. 59).

ECHAM LGM dust fluxes in the Southern Ocean are higher than ACCESS present-day fluxes by, on average, a factor of  $11.4 \pm 6.6$  (Extended Data Fig. 8b). These factors are consistent with the glacial-interglacial difference between ECHAM LGM and pre-industrial fluxes (from the same model)<sup>27</sup>, as well as differences assumed in model studies simulating the biological response to glacial dust<sup>7,20,21</sup>.

### Dust regimes and regional masks

We defined 50 present-day dust regimes on the basis of upper and lower annual mean climatological dust flux limits ( $\text{mg m}^{-2} \text{d}^{-1}$ , ACCESS-AM2). Dust regimes are assumed to be influenced by varying amounts of dust deposition throughout the productive period. The regional extents of each regime are shown in Extended Data Fig. 1 and the respective dust flux limits are specified in the panel titles. Regime limits were set to increase exponentially with increasing distance from the dust source regions, accounting for the nonlinear distribution of dust across the study region (Fig. 1b), to ensure that regimes cover similar areas. Regime limits were allowed to overlap to increase the number of regimes while ensuring that regimes include sufficient float observations for the regime-specific nitrate drawdown analysis.

We applied three regional masks, limiting our study region to the pelagic Southern Ocean south of the nitrate-limited subtropical waters and north of the marginal ice zone: a nitrate limitation mask ( $\text{NO}_3^-$ :chlorophyll less than  $20 \text{ mol g}^{-1}$ )<sup>60</sup>, a sea-ice mask (seasonal maximum sea-ice extent, September sea-ice concentration more than 15%) and a shallow bathymetry mask (water depth less than 2,000 m). The three masks, depicted in Fig. 1a, were used to avoid biases due to nitrate or light limitation and ice-derived, upwelled or sedimentary iron supply. For the calculation of the nitrate limitation mask limits, we used spatially resolved nitrate data which were obtained from the biogeochemical Southern Ocean State Estimate (B-SOSE)<sup>61</sup>, iteration 139, 2013–2021, monthly,  $0.17^\circ \times 0.17^\circ$  spatial resolution, obtained from <http://sose.ucsd.edu/SO6/ITER139/> and remotely sensed surface chlorophyll concentrations by the Visible Infrared Radiometer Suite (VIIRS) aboard the Suomi National Polar-orbiting Partnership (Suomi-NPP) ocean colour satellite. 2012–2021 annual average chlorophyll maps (level 3, mapped,  $0.08^\circ \times 0.08^\circ$  spatial resolution) were obtained from the NASA Ocean Biology Distributed Active Archive Center (OB.DAAC, <https://oceandata.sci.gsfc.nasa.gov/directdataaccess/Level-3%20Mapped/SNPP-VIIRS>). The  $\text{NO}_3^-$ :chlorophyll index was calculated from annual nitrate and chlorophyll climatologies interpolated onto a consistent spatial grid. We defined the nitrate limitation threshold slightly above the proposed literature value of  $17 \text{ mol NO}_3^- (\text{g chlorophyll})^{-1}$  to exclude float observations in regions which potentially shift from iron- to nitrate-limited during the productive period. Sea-ice concentration data were obtained from the same B-SOSE iteration as the surface nitrate data.

### Monthly nitrate climatologies

For each of the 50 dust regimes we calculated 12 depth-resolved monthly nitrate climatologies (January–December) from monthly binned BGC-Argo nitrate profiles measured within the dust-regime boundaries between 2012 and 2022 (Extended Data Fig. 1). All nitrate profiles were interpolated onto a uniform vertical grid from 0 to 1,000 m at 1 m increments before calculating the climatological average. A 3-month running mean was applied to increase the number of observations per monthly climatological average (for example, the February climatology also includes January and March observations). Monthly nitrate climatologies of each dust regime are depicted in Extended Data Fig. 2.

### Regime-averaged ANCP and dust flux

We calculated 50-m- and 200-m-integrated ANCP ( $\text{mol C m}^{-2} \text{yr}^{-1}$ ) in each dust regime from the seasonal annual nitrate drawdown

# Article

$(\Delta\text{NO}_3, \text{mmol NO}_3 \text{ m}^{-2} \text{ yr}^{-1})$  following a method previously used by refs. 26,31.  $\Delta\text{NO}_3$  was calculated over the productive period, defined as the period between the winter nitrate maximum month to the summer minimum month. The productive period is variable across dust regimes but consistent within 2–3 months in most regimes (Extended Data Fig. 3b). The nitrate drawdown throughout the productive period is assumed to be equivalent to the annual nitrate consumption by phytoplankton (assuming negligible growth in autumn and winter) and its rate of change is therefore expressed per year.  $\Delta\text{NO}_3$  was integrated to 50 m and 200 m ( $z_{\text{int}}$ ), calculated as the column-integrated difference between the depth-resolved ( $z$ ) winter maximum and the summer minimum nitrate concentration:

$$\Delta_{z_{\text{int}}}\text{NO}_3 = \int_{0\text{m}}^{z_{\text{int}}} ([\text{NO}_3]_{\text{winter}}(z) - [\text{NO}_3]_{\text{summer}}(z)) \times dz \quad (1)$$

Note that the seasonal nitrate depletion ( $\mu\text{M}$ ), plotted in Fig. 2 and Extended Data Figs. 2 and 3a, refers to the 50-m-averaged nitrate difference. The 50-m-depth limit is equivalent to the median January mixed layer depth (MLD, 49.6 m), computed from float-based CTD observations at each profile location ( $0.03 \text{ kg m}^{-3}$  density threshold criterion<sup>62</sup>).

ANCP ( $\text{mol C m}^{-2} \text{ yr}^{-1}$ ) integrated to 50 and 200 m was computed from  $\Delta\text{NO}_3$  using a Redfield C:N ratio<sup>30</sup> of 106:16 mol mol<sup>-1</sup>.

$$\text{ANCP}_{z_{\text{int}}} = \Delta_{z_{\text{int}}}\text{NO}_3 \times \frac{106 \text{ mol C}}{16,000 \text{ mmol NO}_3} \quad (2)$$

We then matched up the ANCP value of each dust regime with a corresponding seasonally averaged dust deposition ( $\text{mg m}^{-2} \text{ d}^{-1}$ ), calculated as the mean dust deposition at each float profile taken during the productive period (obtained from a monthly ACCESS dust climatology). Note that the regime-specific dust flux is not equal to the midpoint of the regime limits. The uncertainty of the dust flux was propagated from the standard deviation of the dust climatology and is shown as horizontal error bars in Fig. 3.

## Regional ANCP and dust flux variability estimates

To estimate the regional variability of ANCP in each dust regime, we calculated 100 subregional ANCP estimates in the same way described above, by dividing each monthly nitrate climatology into 50 longitude subsets and 50 latitude subsets. These subsets were created using a sliding percentile window, subsampling 20% of the float observations in each monthly climatology bin from east to west and from north to south. This means that subset 1 is based on the westernmost 20% of nitrate observations in each monthly climatological bin through to subset 50, which is based on the easternmost 20% of float observations. Accordingly, subsets 51 through 100 are based on the northernmost to the southernmost 20% of float observations. The standard deviation of all subregional ANCP estimates calculated for each dust regime was taken as the uncertainty of the regime-averaged ANCP and is depicted as vertical error bars in Fig. 3.

This approach was chosen instead of propagating uncertainties from the standard deviations of the nitrate climatologies, which yields unrealistically large uncertainties. Owing to the strong meridional variability of nitrate in the study region, the nitrate climatologies are associated with very high standard deviations. The seasonal nitrate drawdown and ANCP, however, are not expected to be affected by the variability of surface nitrate concentrations, assuming that nitrate is always available in abundance.

## Statistical analysis

We calculated two type-II linear regression models through regime-averaged seasonal dust fluxes and, respectively,  $\text{ANCP}_{50\text{m}}$  and  $\text{ANCP}_{200\text{m}}$ . Because our observations indicate that ANCP increases with dust only where dust fluxes are less than  $7 \text{ mg m}^{-2} \text{ d}^{-1}$ , we calculated the regression

models only through seasonal dust fluxes and corresponding ANCP estimates below this threshold. Above this threshold,  $\text{ANCP}_{50\text{m}}$  remains constant, which we accounted for accordingly in the  $\text{ANCP}_{50\text{m}}$  versus dust model (equation (3)). Regions affected by the high-dust–ANCP limit are indicated by blue and white dots in Fig. 4. We refrained from calculating  $\text{ANCP}_{200\text{m}}$  at more than  $7 \text{ mg m}^{-2} \text{ d}^{-1}$  (equation (4)) because of the uncertainty associated with the observed decline in 200-m-integrated ANCP at high dust.  $R^2$  and  $P$  values were calculated to assert the statistical significance of the regression models and the amount of variability explained. We assume regression confidence intervals of 2 standard deviations ( $\pm 2\sigma$ , indicated by the shades around the regression fits in Fig. 3).

$$\text{ANCP}_{50\text{m}} = \begin{cases} (0.37 \pm 0.03) \times \text{dust} + (0.70 \pm 0.09), & \text{dust} < 7 \\ (0.37 \pm 0.03) \times 7 + (0.70 \pm 0.09), & \text{dust} \geq 7 \end{cases} \quad (3)$$

$$\text{ANCP}_{200\text{m}} = \begin{cases} (1.07 \pm 0.16) \times \text{dust} + (1.30 \pm 0.42), & \text{dust} < 7 \\ \text{not calculated}, & \text{dust} \geq 7 \end{cases} \quad (4)$$

To assess the influence of other environmental parameters on these regressions (mixing, insolation and temperature) we calculated linear regressions between ANCP and the regime-averaged (1) seasonal mean mixed layer depth, (2) seasonal shoaling of the mixed layer, (3) latitude and (4) 50- and 200-m-averaged temperature (Extended Data Fig. 5). These regressions yielded statistically insignificant ( $P > 0.05$ ) or several magnitudes less significant relationships compared to that between ANCP and dust ( $P_{\text{ANCP/dust}} \ll P_{\text{ANCP/param}} < 0.05$ ). Furthermore, we calculated two multiple linear regressions using  $\text{ANCP}_{50\text{m}}$  and  $\text{ANCP}_{200\text{m}}$  as the respective responses and environmental parameters 1–4 alongside dust as predictors, which yielded the same ANCP/dust slope and uncertainties as the univariate regressions (equations (3) and (4)) and markedly lower  $P$  values associated with dust compared to the other environmental predictors. These analyses indicate that the basin-scale increasing  $\text{ANCP}_{50\text{m}}$  and  $\text{ANCP}_{200\text{m}}$  gradient across dust regimes is driven largely by dust and well represented by the univariate ANCP–dust-regression models.

## Dust-derived ANCP maps and dust contribution

We used equations (3) and (4) to derive spatially resolved 50- and 200-m-integrated ANCP ( $\text{gC m}^{-2} \text{ yr}^{-1}$ ) south of  $30^\circ \text{S}$  from simulated present-day and LGM dust deposition maps (ACCESS-AM2 and ECHAM6). The percentage dust contribution ( $\kappa$ ) to  $\text{ANCP}_{50\text{m}}$  and  $\text{ANCP}_{200\text{m}}$ , representing the fraction of ANCP supported by dust-iron addition, was calculated as

$$\kappa_{z_{\text{int}}} = \frac{\text{ANCP}_{z_{\text{int}}} - \text{ANCP}_{\text{BG},z_{\text{int}}}}{\text{ANCP}_{z_{\text{int}}}}, \quad (5)$$

where  $\text{ANCP}_{\text{BG}}$  (background ANCP) is equal to the  $y$  intercept of the respective regression (equations (3) and (4)) and assumed to be constant, reflecting ANCP in the absence of dust.

In the calculation of ANCP maps, we abandoned the nitrate limitation mask and instead applied a nitrate limitation correction, both to present-day and LGM ANCP maps, to account for nitrate depletion and limitation of productivity during the productive period, regardless of continuing dust-iron supply. To this end, we calculated spatially resolved upper thresholds of  $\text{ANCP}_{50\text{m}}$  ( $\text{ANCP}_{\text{max}}$ ) (Extended Data Fig. 7) across the Southern Ocean south of  $30^\circ \text{S}$  from a B-SOSE winter surface nitrate climatology (August/September,  $[\text{NO}_3]_{\text{winter,BSOSE}}$ ):

$$\text{ANCP}_{\text{max}} = \int_{0\text{m}}^{50\text{m}} [\text{NO}_3]_{\text{winter,BSOSE}}(z) \times \frac{106 \text{ mol C}}{16,000 \text{ mmol NO}_3} \times 12 \frac{\text{g}}{\text{mol}}. \quad (6)$$

$\text{ANCP}_{\max}$  is assumed to be the maximum possible  $\text{ANCP}_{50m}$  that can be supported by the nitrate inventory in the upper 50 m at the start of the productive period. Note that nitrate is assumed to be potentially limiting only above 50 m, whereas below 50 m, where nitrate concentrations increase and productivity decreases, nitrate is assumed to be always available in abundance. Therefore, in the  $\text{ANCP}_{200m}$  maps, the nitrate limitation cap is only applied above 50 m. The nitrate limitation cap was applied as follows:

$$\text{ANCP}_{\text{exc}} = \begin{cases} \text{ANCP}_{50m} - \text{ANCP}_{\max}, & \text{ANCP}_{50m} > \text{ANCP}_{\max} \\ 0, & \text{ANCP}_{50m} < \text{ANCP}_{\max} \end{cases} \quad (7)$$

$$\text{ANCP}_{\text{Nlim}, z_{\text{int}}} = \text{ANCP}_{z_{\text{int}}} - \text{ANCP}_{\text{exc}}, \quad (8)$$

where  $\text{ANCP}_{\text{exc}}$  refers to amount of  $\text{ANCP}_{50m}$  derived from dust (equation (3)) that exceeds  $\text{ANCP}_{\max}$  and  $\text{ANCP}_{\text{Nlim}, z_{\text{int}}}$  refers to  $\text{ANCP}_{50m}$  and  $\text{ANCP}_{200m}$  corrected for nitrate limitation above 50 m. The nitrate limitation cap, indicated by red and white dots in Fig. 4, was applied both to present-day and LGM ANCP maps.

By applying the regression model, which is constrained to the subantarctic zone, to low-nitrate subtropical regions in conjunction with the nitrate limitation cap, we assume that, as long as nitrate is not limiting, the biological response to dust-iron is consistent throughout the Southern Ocean south of 30° S.

Basin-integrated ANCP estimates ( $\text{PgC yr}^{-1}$ ) presented in the main text were spatially integrated across the pelagic, ice-free Southern Ocean south of 30° S omitting values in regions masked out by the sea-ice mask and the shallow bathymetry mask. Basin-integrated  $\text{ANCP}_{200m}$  estimates also exclude regions exceeding  $7 \text{ mg dust m}^{-2} \text{ d}^{-1}$ . Areas in  $\text{km}^2$  of 50 m and 200 m basin-integrated values are indicated in the captions of Fig. 4 and Extended Data Fig. 6. Uncertainties reported for basin-wide estimates were propagated from the  $2\sigma$  standard deviation of the ANCP versus dust regression models.

### Fe:C uptake ratio

Southern Ocean basin-averaged cellular iron requirements (Fe:C,  $\mu\text{mol (mol)}^{-1}$ ) were inferred from the type-II linear regression slope (Extended Data Fig. 4) ( $P < 10^{-10}$ ,  $R^2 = 0.65$ ) calculated through the regime-averaged daily net community production integrated to 200 m ( $\text{NCP}_{200m}$ ,  $\text{mol C m}^{-2} \text{ d}^{-1}$ ) and dust-derived bioavailable iron fluxes (sFe,  $\mu\text{mol m}^{-2} \text{ d}^{-1}$ ).  $\text{NCP}_{200m}$  was calculated by dividing  $\text{ANCP}_{200m}$  by the duration of the productive period. The sFe was derived from dust deposition fluxes assuming 3.5 wt% iron content in dust<sup>16</sup> and 5–15% fractional iron solubility in seawater<sup>38</sup>. Observations of more than  $7 \text{ mg dust m}^{-2} \text{ d}^{-1}$  were excluded from the regression. Above this threshold, productivity is limited by iron-scavenging and self-shading (main text), which biases Fe:C uptake ratios. The inverse of the  $\text{NCP}_{200m}$  versus sFe regression slope yields Fe:C ratios ranging from 5 to 15  $\mu\text{mol Fe (mol C)}^{-1}$ , assuming that dust-iron is completely converted to phytoplankton-biomass, where dust fluxes are less than  $7 \text{ mg dust m}^{-2} \text{ d}^{-1}$ .

### Temperature limitation factors

Temperature limitation factors ( $T_{\text{lim}}$ ) are commonly used in phytoplankton ecosystem models to parameterize the limitation of growth below 30 °C water temperature<sup>63</sup> and can be calculated using the equation  $T_{\text{lim}} = Q_{10}^{\left(\frac{T-30}{10}\right)}$ , where  $Q_{10} = 2$ .  $Q_{10}$  represents a doubling of growth rates per 10 °C at the reference temperature of 30 °C.  $T_{\text{lim}}$  yields a fraction ( $0 < T_{\text{lim}} < 1$ ) by which the growth rate is limited at temperatures less than 30 °C, where lower values indicate stronger temperature limitation of productivity. We calculated  $T_{\text{lim}}$  at the maximum and minimum observed water temperatures across all dust regimes, averaged seasonally and above 50 m and 200 m (Extended Data Fig. 5a,d). The ratio of  $T_{\text{lim}}$  at both ends of the basin-wide temperature range was

taken as the maximum productivity increase due to temperatures alone. The percentage difference of  $T_{\text{lim}}$  between dust regimes represents the percentage difference in productivity that can be attributed to changes in temperature alone. The maximum increase in  $T_{\text{lim}}$  between dust regimes is 25–29%, which cannot explain the observed 515% and 1,090% increase in  $\text{ANCP}_{50m}$  and  $\text{ANCP}_{200m}$ .

### Data availability

Supporting data used in the analysis are available at <https://doi.org/10.5281/zenodo.10374127> (ref. 64). ACCESS-AM2 2015–2019 dust fields are available at <https://doi.org/10.5281/zenodo.8303317> (ref. 56). Figures were created in MATLAB and Adobe Illustrator. Source data are provided with this paper.

### Code availability

Analysis scripts are available at <https://doi.org/10.5281/zenodo.10374127> (ref. 64). The ECHAM6-HAMMOZ model code and all required input data are maintained and made available at <https://redmine.hammoz.ethz.ch> after signing a software license agreement that can be downloaded from [https://redmine.hammoz.ethz.ch/attachments/291/License\\_ECHAM-HAMMOZ\\_June2012.pdf](https://redmine.hammoz.ethz.ch/attachments/291/License_ECHAM-HAMMOZ_June2012.pdf).

48. Johnson, K. S. & Coletti, L. J. In situ ultraviolet spectrophotometry for high resolution and long-term monitoring of nitrate, bromide and bisulfide in the ocean. *Deep-Sea Res. I* **49**, 1291–1305 (2002).
49. MacIntyre, G. et al. ISUS/SUNA nitrate measurements in networked ocean observing systems. In *Proc OCEANS 2009* (IEEE, Biloxi, 2009).
50. Johnson, K. S. et al. *Processing Bio-Argo Nitrate Concentration at the DAC Level* (Ifremer, 2018); <https://doi.org/10.13155/46121>.
51. OneArgo-Mat: A MATLAB toolbox for accessing and visualizing Argo data v. 1.0.3. Zenodo <https://doi.org/10.5281/zenodo.6603689> (2022).
52. Johnson, K. S. et al. Biogeochemical sensor performance in the SOCCOM profiling float array. *J. Geophys. Res. Oceans* **122**, 6416–6436 (2017).
53. Bi, D. H. et al. Configuration and spin-up of ACCESS-CM2, the new generation Australian Community Climate and Earth System Simulator Coupled Model. *J. South. Hemisph. Earth Syst.* **70**, 225–251 (2020).
54. Fiddes, S. L., Protat, A., Mallet, M. D., Alexander, S. P. & Woodhouse, M. T. Southern Ocean cloud and shortwave radiation biases in a nudged climate model simulation: does the model ever get it right. *Atmos. Chem. Phys.* **22**, 14603–14630 (2022).
55. Woodward, S. Modeling the atmospheric life cycle and radiative impact of mineral dust in the Hadley Centre climate model. *J. Geophys. Res. Atmos.* **106**, 18155–18166 (2001).
56. Fiddes, S. L. ACCESS-AM2 dust fields 2015–2019 [data set]. Zenodo <https://doi.org/10.5281/zenodo.8303317> (2023).
57. Stevens, B. et al. Atmospheric component of the MPI-M Earth System Model: ECHAM6. *J. Adv. Model. Earth Syst.* **5**, 146–172 (2013).
58. Schultz, M. G. et al. The chemistry-climate model ECHAM6.3-HAM2.3-MOZ1.0. *Geosci. Model. Dev.* **11**, 1695–1723 (2018).
59. ECHAM6-HAMMOZ model data (HAMMOZ, accessed 14 September 2020); <https://redmine.hammoz.ethz.ch/projects/hammoz/repository/1/show/echam6-hammoz/branches/tanja>.
60. Basterretxea, G., Font-Muñoz, J. S., Hernández-Carrasco, I. & Sañudo-Wilhelmy, S. A. Global variability of high-nutrient low-chlorophyll regions using neural networks and wavelet coherence analysis. *Ocean Sci.* **19**, 973–990 (2023).
61. Verdy, A. & Mazloff, M. R. A data assimilating model for estimating Southern Ocean biogeochemistry. *J. Geophys. Res. Oceans* **122**, 6968–6988 (2017).
62. Holte, J. & Talley, L. A new algorithm for finding mixed layer depths with applications to Argo data and subantarctic mode water formation. *J. Atmos. Ocean Tech.* **26**, 1920–1939 (2009).
63. Krumhardt, K. M., Long, M. C., Sylvester, Z. T. & Petrik, C. M. Climate drivers of Southern Ocean phytoplankton community composition and potential impacts on higher trophic levels. *Front. Mar. Sci.* **9**, 916140 (2022).
64. Weis, J. Code repository for “One-third of Southern Ocean productivity is supported by dust deposition”. Zenodo <https://doi.org/10.5281/zenodo.10374127> (2024).
65. Frank, M. et al. Similar glacial and interglacial export bioproductivity in the Atlantic sector of the Southern Ocean: multiproxy evidence and implications for atmospheric CO<sub>2</sub>. *Paleoceanogr. Paleoclimatol.* **15**, 642–658 (2000).
66. Nürnberg, C. C., Bohrmann, G., Frank, M. & Schlüter, M. Barium accumulation in the Atlantic sector of the Southern Ocean—results from 190,000 year records. *Paleoceanogr. Paleoclimatol.* **12**, 594–603 (1997).
67. Lamy, F. et al. Increased dust deposition in the Pacific Southern Ocean during glacial periods. *Science* **343**, 403–407 (2014); <https://doi.org/10.1126/science.1245424>.
68. Toyos, M. H. et al. Concentration, accumulation rates, Th fluxes, focusing factors and productivity proxies on core PS97/093-2 over the past 400,000 years. PANGAEA <https://doi.org/10.1594/PANGAEA.934588> (2021).

# Article

69. Thöle, L. M. et al. Glacial–interglacial dust and export production records from the Southern Indian Ocean. *Earth Planet. Sci. Lett.* **525**, 115716. (2019).

**Acknowledgements** We would like to acknowledge the Argo Program, which is part of the Global Ocean Observing System (<https://www.searoe.org/data/0031142182/>), the Southern Ocean Observing System (SOOS) and the Southern Ocean Carbon and Climate Observations and Modeling (SOCCOM) Project funded by the National Science Foundation, Division of Polar Programs (NSF PLR-1425989 and OPP-1936222), supplemented by NASA. The BGC-Argo data were collected and made freely available by the International Argo Program and the national programmes that contribute to it (<http://www.argo.ucsd.edu>, <http://argo.jcommops.org>). This research was undertaken with the assistance of resources and services from the National Computational Infrastructure (project jk72), which is supported by the Australian Government. This research was partially funded by the Australian Government through the Australian Research Council's Discovery Projects funding scheme (project DP190103504). A.R.B. and S.L.F. are supported by the Australian Antarctic Program Partnership (AAPP) as part of the Antarctic Science Collaboration Initiative (ASCI000002). J.W. and P.G.S. are also supported by the Australian Research Council Centre of Excellence for Climate Extremes (CLEX, CE170100023).

We thank S. Krätschmer for providing the LGM dust deposition simulations used in this study. We thank M. Mazloff and T. Rohr for their valuable insights and constructive feedback.

**Author contributions** J.W., Z.C., C.S., P.G.S. and A.R.B. conceived the study. J.W. conducted the analysis and wrote the manuscript with contributions from all co-authors. S.L.F. provided ACCESS dust deposition model outputs. All authors contributed to the interpretation of the results.

**Competing interests** The authors declare no competing interests.

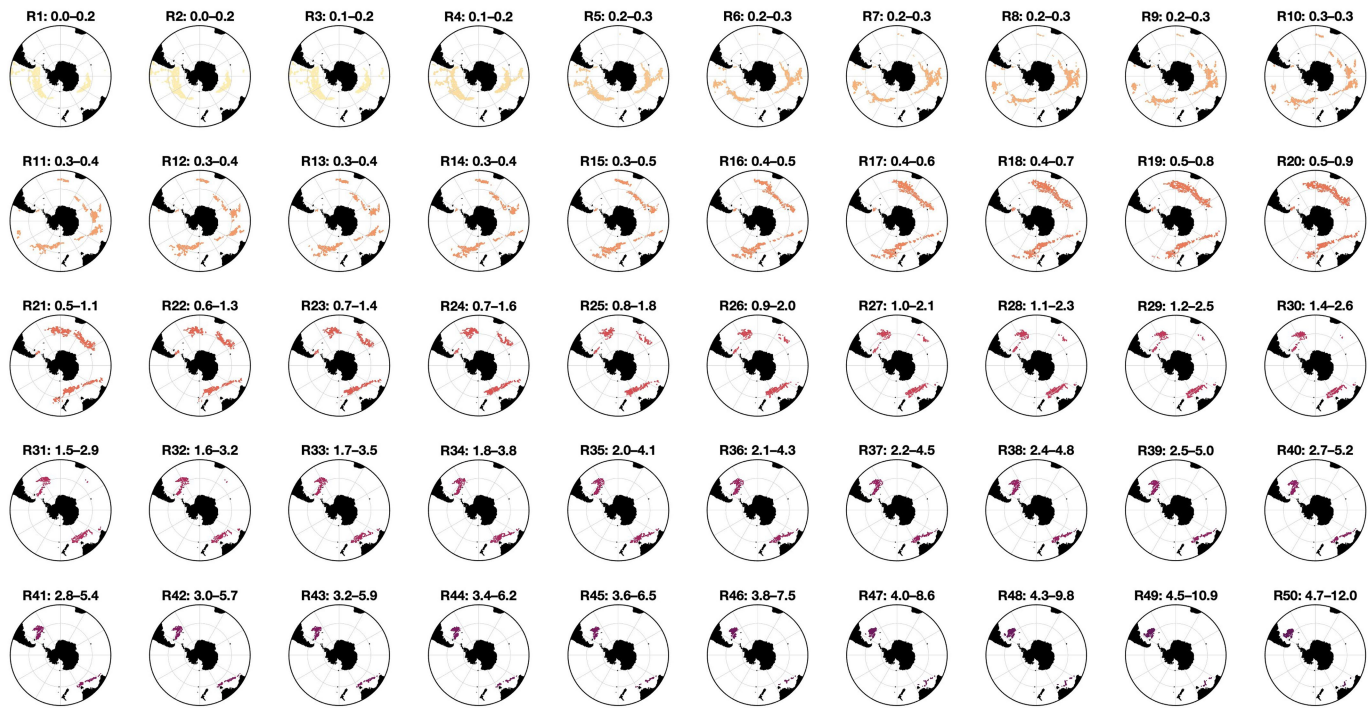
## Additional information

**Supplementary information** The online version contains supplementary material available at <https://doi.org/10.1038/s41586-024-07366-4>.

**Correspondence and requests for materials** should be addressed to Jakob Weis.

**Peer review information** *Nature* thanks Mathis Hain and the other, anonymous, reviewer(s) for their contribution to the peer review of this work.

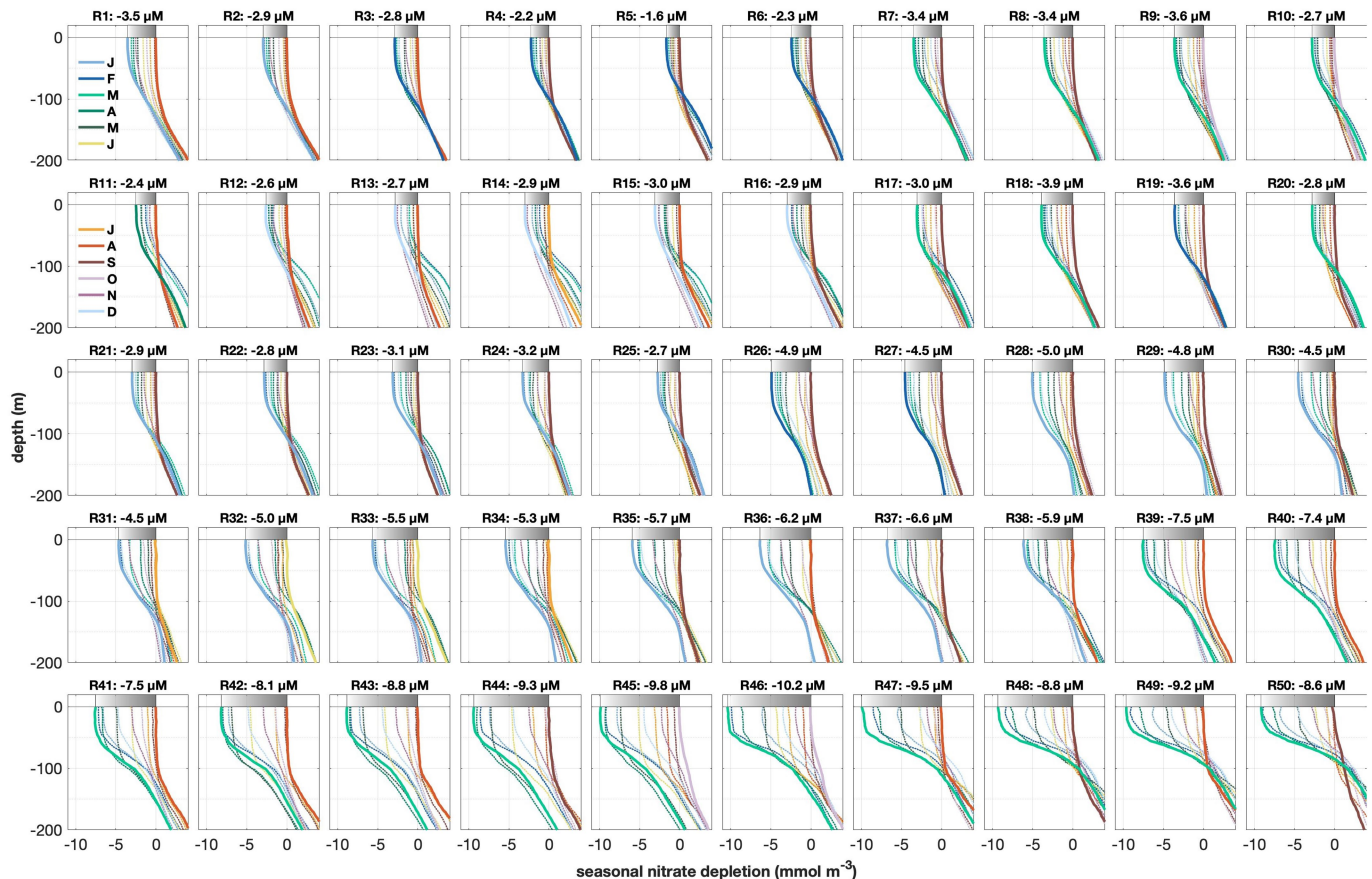
**Reprints and permissions information** is available at <http://www.nature.com/reprints>.



**Extended Data Fig. 1 | Regional extents of the 50 dust regimes.** The 50 dust regimes (R1–R50) defined in this study from low dust (top left) to high dust deposition (bottom right) and 2012–2022 BGC-Argo nitrate observations included in each regime. Lower and upper annual mean dust flux limits ( $\text{mg m}^{-2} \text{d}^{-1}$ ) delineating each regime are indicated in the titles. Note that dust

regime boundaries are partially overlapping. Dust limits increase exponentially from low-dust to high-dust regimes, due to the exponential decline of dust with distance from the source regions (see Fig. 1b), ensuring that regimes are similar in regional extent and number of float observations.

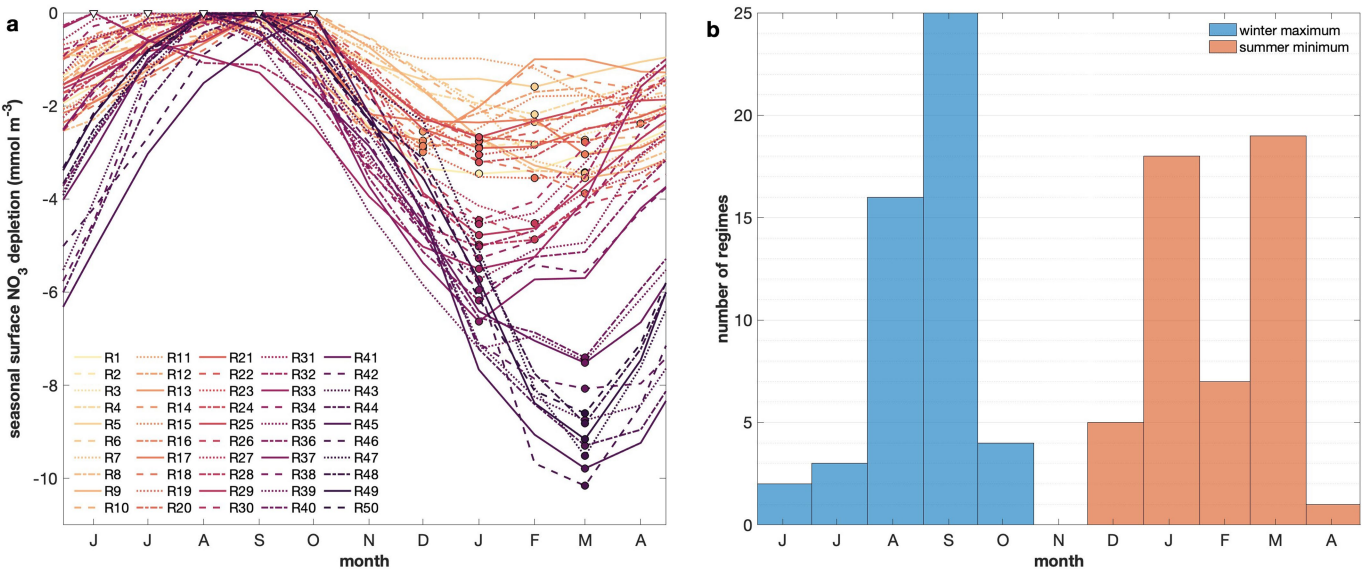
# Article



**Extended Data Fig. 2 | Monthly nitrate climatologies of the 50 dust regimes.**

Monthly 0–200 m nitrate climatologies calculated from float observations in each of the 50 dust regimes (Extended Data Fig. 1). Plotted on the x-axis is the difference in nitrate concentration relative to the winter surface nitrate

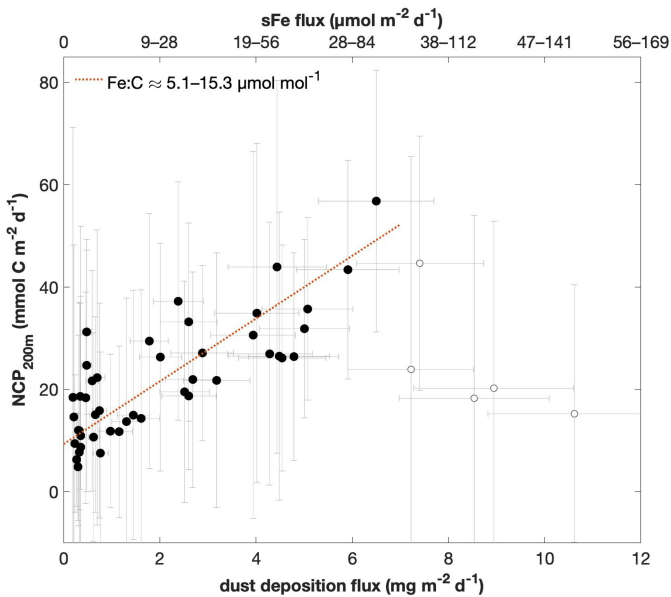
maximum, illustrating the seasonal nitrate depletion in the epipelagic zone. The horizontal grey bar above each panel indicates the 50-m-averaged maximum seasonal nitrate difference between the winter maximum to the summer minimum (solid profiles, drawdown values are indicated in the title).



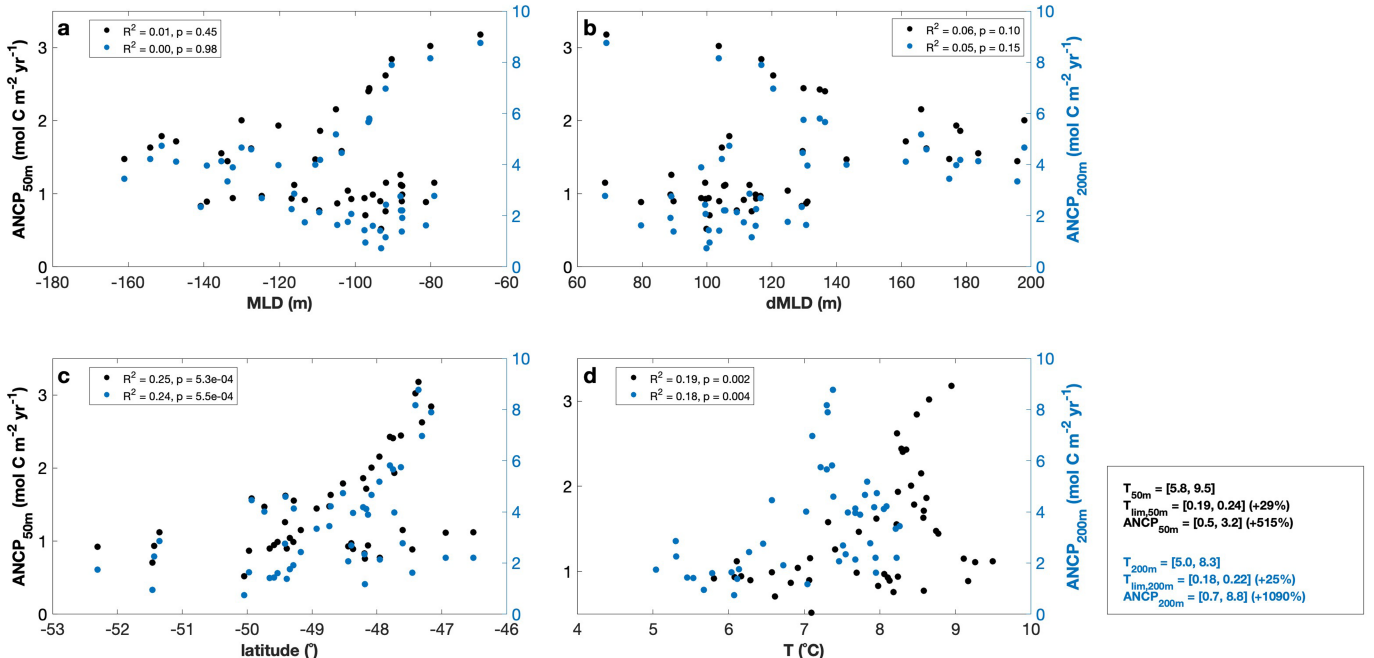
#### Extended Data Fig. 3 | Surface nitrate seasonality in each dust regime.

**a**, 50-m-mean surface nitrate depletion between the seasonal surface nitrate maximum (triangles) and minimum (circles) in each of the 50 dust regimes (Extended Data Fig. 1). **b**, Histogram of the winter nitrate maximum (blue bars)

and summer minimum months (red bars), defining the start and end of the productive period, in each dust regime. In >80% of the regimes, the productive period begins in August or September (41 out of 50) and ends between January and March (44 out of 50).

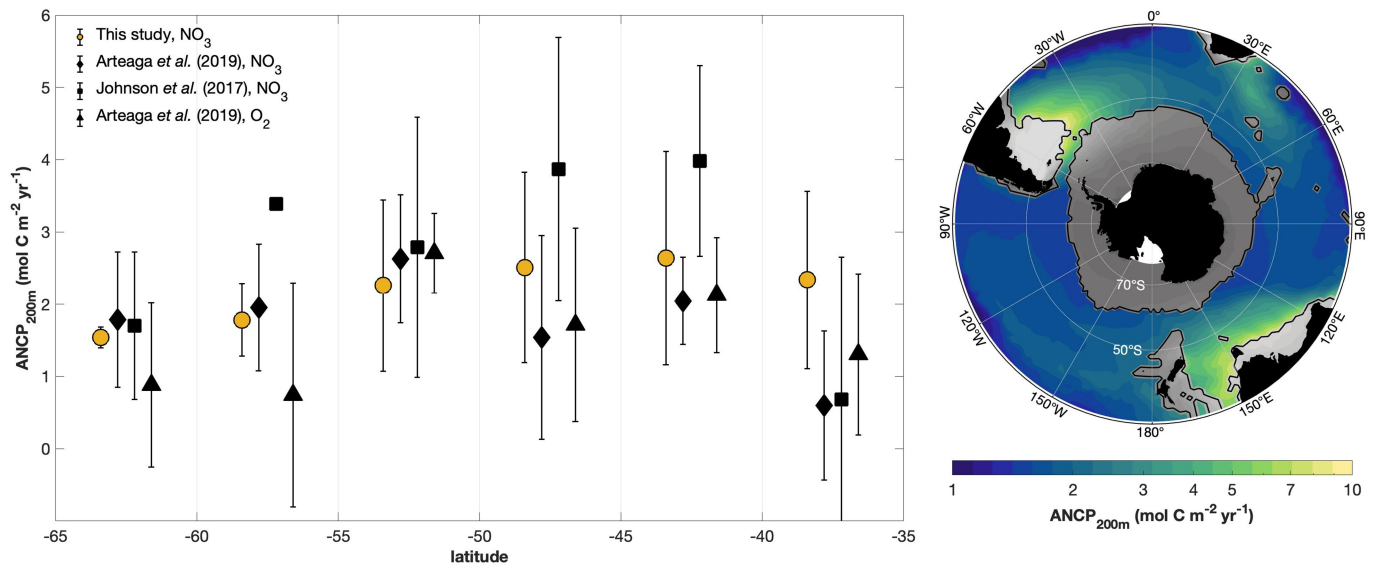


**Extended Data Fig. 4 | Fe:C ratios derived from net community production and dust-derived soluble iron fluxes.** 200-m-integrated net community production ( $\text{NCP}_{200m} = \text{ANCP}_{200m}$  divided by the productive period length) regressed against dust deposition fluxes (lower x-axis) in each of the 50 dust regimes. Southern Ocean basin-averaged Fe:C uptake ratios, indicated in the key, were inferred from the inverse of the regression slope (dotted line) and bioavailable soluble iron (sFe) fluxes (upper x-axis, derived from dust using 3.5 weight-% dust-iron content<sup>16</sup> and 5–15% fractional iron solubility<sup>38</sup>). Observations exceeding 7  $\text{mg dust m}^{-2} \text{d}^{-1}$  (open markers) were excluded from the regression and the Fe:C calculation due to the assumed limitation of productivity by iron-scavenging and self-shading on NCP under high dust loads. See the methods for further information.



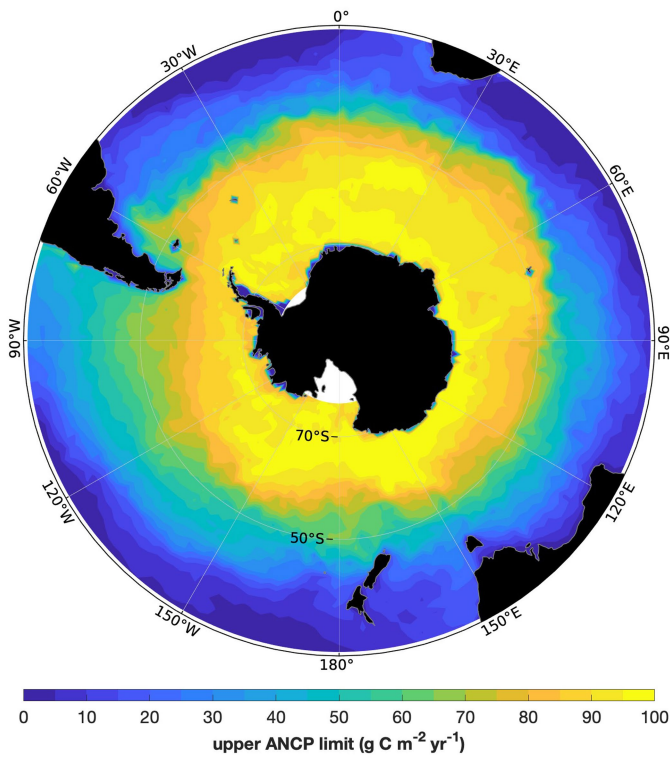
**Extended Data Fig. 5 | Covariance analysis between ANCP and mixing, latitude and temperature.** Linear regressions of  $\text{ANCP}_{50\text{m}}$  (black, left y-axis) and  $\text{ANCP}_{200\text{m}}$  (blue, right y-axis) against, **a**, seasonal mean mixed layer depths, **b**, the seasonal shoaling of the mixed layer, **c**, latitude and, **d**, seasonal mean temperatures (50 and 200-m-averaged).  $R^2$  and p-values are indicated in the key. ANCP increases northwards, whereas insolation decreases northwards during the productive period (austral spring and summer). Furthermore, the

insolation difference in the observed latitude range is minor, which precludes a direct influence of light on the observed increase in ANCP. Temperature limitation factors ( $T_{\text{lim}}$ , box next to panel e) were calculated to estimate the maximum possible temperature-induced increase in productivity across dust regimes (see methods), indicating that temperature differences can only account for a minor fraction of the observed ANCP increase.


**Extended Data Fig. 6 | Latitudinally binned 200-m-integrated ANCP.**

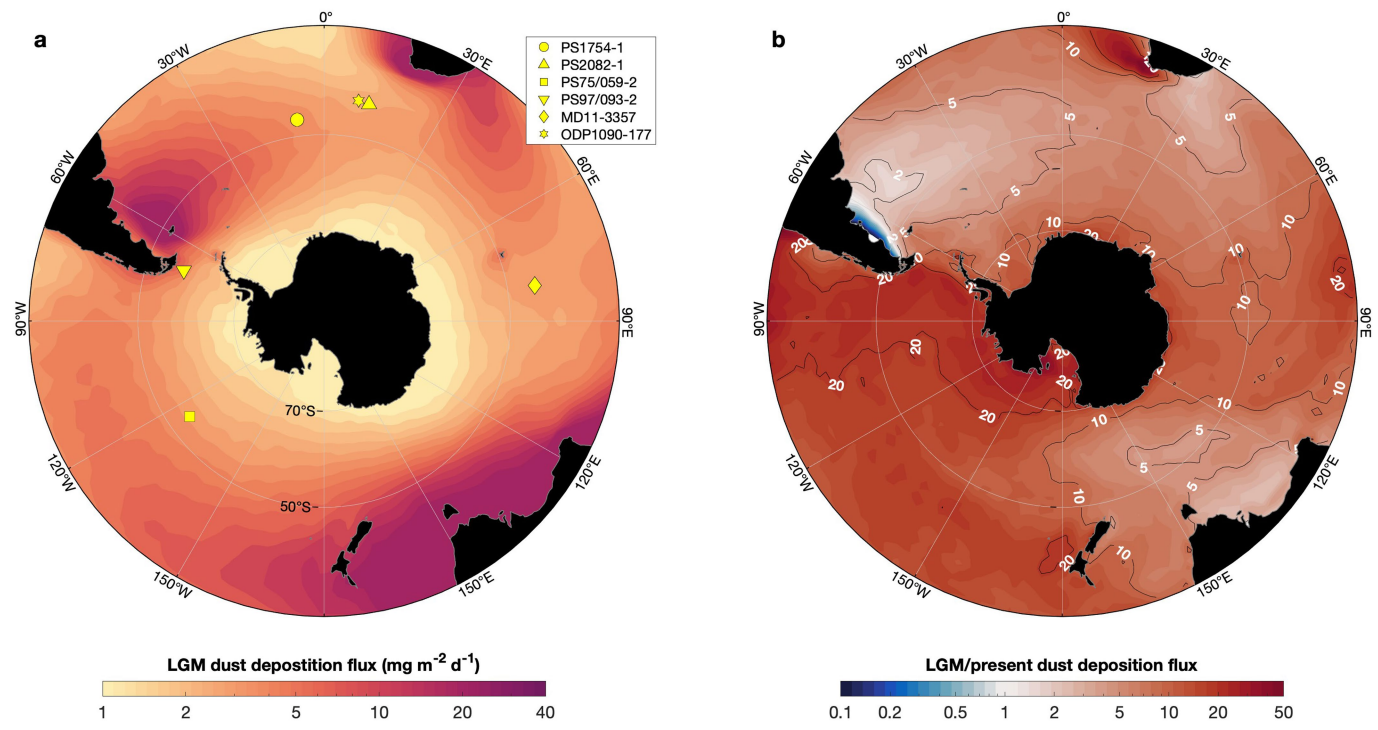
$\text{ANCP}_{200\text{m}}$  averaged over  $5^\circ$  latitudinal bins from this study (yellow markers, mapped on the right) compared against corresponding literature values<sup>26,31</sup> (black markers). Each set of markers refers to the same  $5^\circ$  latitude bin indicated by the x-axis ticks. Oxygen-derived ANCP estimates from Arteaga, et al.<sup>31</sup> were calculated based on respiration rates integrated from 100 to 500 m. Regions

accounted for in the latitudinally binned and basin-integrated estimates reported in the main text, highlighted in colour, exclude the sea ice zone, shelf regions and high dust regions ( $> 7 \text{ mg dust m}^{-2} \text{ d}^{-1}$ ) and cover 76 million  $\text{km}^2$ . High dust regions were excluded due to the uncertainty associated with the decline of  $\text{ANCP}_{200\text{m}}$  in these regions (see Fig. 3).



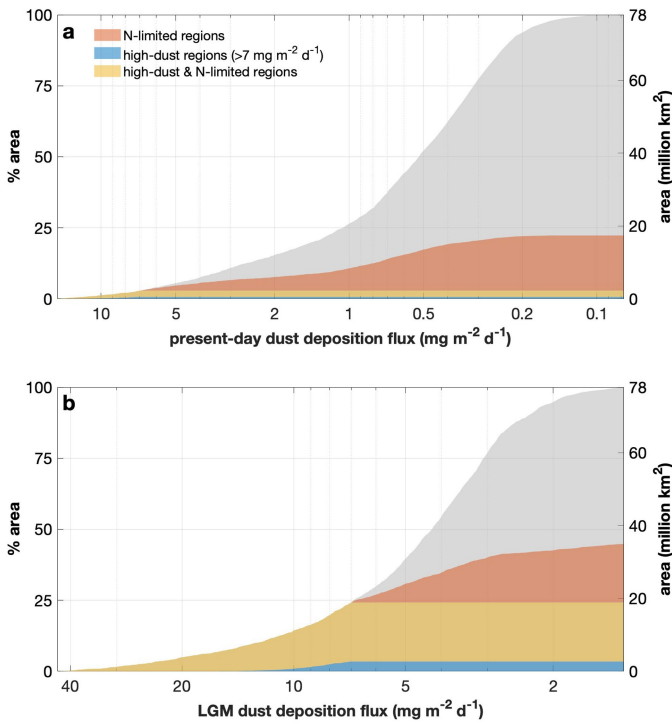
#### Extended Data Fig. 7 | Maximum ANCP supportable by the winter nitrate inventory.

**inventory.** Upper ANCP limit ( $\text{ANCP}_{\text{max}}$  in equation 6), derived from the 50-m-integrated winter nitrate inventory at the start of the productive period (August/September climatology, 2013–2021 B-SOSE<sup>61</sup>). These values are considered to be the upper limit of  $\text{ANCP}_{50m}$  before productivity is limited by nitrate and cannot be further sustained by dust-iron addition (see Methods).  $\text{ANCP}_{\text{max}}$  values were used to cap present-day and LGM ANCP estimates in high-dust and low-nitrate regions, respectively. Adjusted regions are indicated by red and white dots in Fig. 4.



**Extended Data Fig. 8 | ECHAM6.3 simulated LGM dust deposition fluxes and difference relative to present-day fluxes.** **a**, Southern Ocean dust deposition fluxes during the Last Glacial Maximum (LGM) obtained from the ECHAM6.3-HAM2.3 coupled atmosphere-aerosol model<sup>27</sup>. Markers indicate

sediment core locations referred to in Extended Data Table 1. **b**, LGM dust fluxes divided by ACCESS-AM2 present-day dust fluxes mapped in Fig. 1b. Across the pelagic ice-free Southern Ocean, ECHAM LGM dust fluxes are, on average, by a factor of  $11.4 \pm 6.6$  higher than ACCESS present-day dust fluxes.



**Extended Data Fig. 9 | Cumulative areas impacted by dust, nitrate limitation and high dust loads.** The grey shades indicate the cumulative area of, **a**, present-day and, **b**, LGM dust influence on the Southern Ocean with decreasing dust deposition, illustrating the expansion of dust from the source regions. The total area of the study region, the pelagic ice-free Southern Ocean south of  $30^\circ \text{S}$ , is 78 million  $\text{km}^2$ . The overlayed blue, red and yellow shades indicate, respectively, the cumulative area that is impacted by nitrate limitation, high dust loads ( $> 7 \text{ mg m}^{-2} \text{ d}^{-1}$ ), or both. Therefore, the blue and yellow shade combined represent high-dust regions and the red and yellow shade combined represent nitrate-limited regions.

# Article

**Extended Data Table 1 | Glacial–interglacial productivity variability comparison**

Core Site	Basin	LGM to present day ratio	
		Proxy record	This study
PS1754-1, <sup>64</sup>	Atlantic	1.6±0.2*, 2.3±0.4 <sup>†</sup>	1.9±0.2
PS2082-1, <sup>65</sup>	Atlantic	2.1±0.8*	1.9±0.2
ODP1090-177, <sup>3</sup>	Atlantic	1.5±0.6 <sup>‡</sup>	1.8±0.2
PS75/059-2, <sup>66</sup>	Pacific	1.4±0.1*, 1.6±0.5 <sup>§</sup>	2.3±0.3
PS97/093-2, <sup>67</sup>	Pacific	2.6±0.2*, 4.9±0.4 <sup>¶</sup>	3.5±0.5
MD11-3357, <sup>68,69</sup>	Indian	1.1±0.1 <sup>§</sup> , 2.5±0.9 <sup>¶</sup>	2.2±0.3

\*Barium excess ( $Ba_{exc}$ ), Th-normalised flux

<sup>†</sup>Beryllium-10 ( $^{10}Be$ ), Th-normalised flux

<sup>‡</sup>Bulk nitrogen, Th-normalised flux

<sup>§</sup>Opal, Th-normalised flux

<sup>¶</sup>Total organic carbon (TOC), Th-normalised flux

LGM to present-day export production ratio derived from sediment proxy records in the three Southern Ocean basins. Proxy-derived ratios are compared to ratios calculated from present-day and LGM ANCP<sub>50m</sub>, derived from the ANCP<sub>50m</sub> vs. dust regression model, at the respective core locations indicated in Extended Data Fig. 8. All sediment cores were taken in the subantarctic zone. Proxy record ratios were calculated between the most recent observation and the mean ( $\pm 1\sigma$ ) of observations between 15 and 25 ka. The specific sediment proxies the ratios are based on are listed in the footnotes<sup>65–69</sup>.